OPTICAL FIBER SENSORS FOR DAMAGE ANALYSIS IN AEROSPACE MATERIALS

NASA Langley Research Center
GRANT NAG-1-1508

FINAL REPORT
August 1, 1993 - December 31, 1995

Submitted to: Dr. Robert Rogowski
NASA Langley Research Center
MS 231
Hampton, VA 23665

Submitted by: Paul Schindler
Russell May, co-PI
Richard Claus, co-PI
Fiber & Electro-Optics Research Center
Bradley Department of Electrical Engineering
Virginia Tech
Blacksburg, VA 24061-0111

Fiber & Electro-Optics
RESEARCH CENTER

TABLE OF CONTENTS

TABLE OF FIGURES

TABLE OF TABLES

1.0 Overview

As the average age of the nation's aircraft increases, there is an intensifying interest in the development of tools and techniques that may be used to assess the structural health of aging aircraft. Under this grant, fiber optic sensors were investigated for use in the nondestructive evaluation of aging aircraft. Specifically, optical fiber sensors for detection and location of impacts on a surface, and for detection of corrosion in metals were developed.

The use of neural networks was investigated for determining impact location by processing the output of a network of fiberoptic strain sensors distributed on a surface. This approach employs triangulation to determine location by comparing the arrival times at several sensors, of the acoustic signal generated by the impact. For this study, a neural network simulator running on a personal computer was used to train a network using a back-propagation algorithm. Fiber optic extrinsic Fabry-Perot interferometer (EFPI) strain sensors are attached to or embedded in the surface, so that stress waves emanating from an impact can be detected. The ability of the network to determine impact location by time-of-arrival of acoustic signals was assessed by comparing network outputs with actual experimental results using impacts on a panel instrumented with optical fiber sensors. Using the neural network to process the sensor outputs, the impact location can be inferred to centimeter range accuracy directly from the arrival time data. In addition, the network can be trained to determine impact location, regardless of material anisotropy. Results demonstrate that a back-propagation network identifies impact location for an anisotropic graphite/bismaleimide plate with the same accuracy as that for an isotropic aluminum plate.

Two different approaches were investigated for the development of fiber optic sensors for corrosion detection in metals, both utilizing optical fiber sensors with metal coatings. In the first approach, an extrinsic Fabry-Perot interferometric fiber optic strain sensor was placed under tensile stress, and while in the resulting strained position, a thick coating of metal was applied. Due to an increase in the quantity of material, the sensor does not return to its original position upon removal of the applied stress, and some residual strain is maintained within the sensor element. As the metal thickness decreases due to corrosion, this strain is released, providing the sensing mechanism for corrosion detection.

In the second approach, photosensitive optical fibers with long period Bragg gratings in the core were coated with metal. The Bragg gratings serve to couple core modes at discrete wavelengths to cladding modes. Since cladding modes interact with the metal coating surrounding the fiber cladding, the specific wavelengths coupled from core to cladding depend on the refractive index of the metal coating. Therefore, as the metal corrodes, the resulting change in index of the coating may be measured by measuring the change in wavelength of the coupled mode. Results demonstrate that both approaches can be successfully used to track the loss in metal coating on the optical fiber sensors due to corrosion.

2.0 Objective

The objective of this program was the development of practical and cost effective damage sensors for eventual integration into an on-board health monitoring system on civilian and military aircraft and spacecraft. In particular, fiber optic sensors for the detection and location of impacts on a surface, and for detection of corrosion, were investigated and developed.

3.0 Summary of Progress

3.1 Performance Metrics of Optical Fiber Sensors for Health Monitoring

Here we sought to determine quantitative sensor performance goals required by standard aircraft maintenance and repair procedures for:

- minimum detectable fatigue crack length,
- minimum detectable impact energies and maximum impact location error,
- minimum detectable delamination area size, and
- minimum loss of metal resolution for indication of corrosion.

These were determined by reviewing current and potential modified methods for the evaluation of structural damage in aircraft materials. A search for specifications, standards, and documentation that may contain quantitative requirements for aircraft NDE was undertaken. Specifically,

- Federal Aviation Administration (FAA) Advisory Circulars were reviewed at the Virginia Tech airport. Circulars relating to aircraft NDE were identified, ordered from the FAA, and reviewed.

- Military standards and specifications were reviewed at the Virginia Tech library, where they are available on CD-ROM. Standards relating to aircraft NDE were identified and ordered from the federal government.

- A visit was made to the maintenance department of USAir at the Roanoke Regional Airport (Woodrum Field) to visit the maintenance hanger to observe an inspection and maintenance of a USAir aircraft. In addition,

maintenance personnel were on hand to answer questions regarding NDE procedures at USAir.

- Interviews were held with Virginia Tech professors familiar with NDE and materials characterizations. Dr. R.W. Hendricks of the Materials Science and Engineering Department, and Drs. E.G. Henneke and N.E. Dowling of the Engineering Science and Mechanics Department were helpful in suggesting background literature on specific topics in materials NDE (such as crack propagation); they were not able to identify specific quantitative specifications for NDE used by the aircraft industry.

- A literature search was undertaken to find conference and journal papers relating to the four measurands (crack propagation, impact damage, corrosion, and delamination). Several papers were reviewed to determine the current state-of-the-art for those measurements.

In general, we found few specific quantitative specifications for aircraft NDE which could be used to generate performance requirements for optical fiber sensors. A list of related documents that were found to be helpful is given in Section 4, References. Specific citations of quantitative capabilities of NDE inspection techniques from the references are discussed below.

Basic NDE techniques and theory for aircraft inspection are described in the NAVAIR document Nondestructive Inspection Methods.[1] The methods that are described are liquid penetrant (visible dye and fluorescent dye), magnetic particle methods, electromagnetic methods (eddy current and magnetic field), ultrasonic methods, and radiography.

The military specification for aircraft structure damage tolerance analysis, MIL-A-83444, describes general criteria for maximum initial flaw sizes.[2] In particular, for drilled fastener holes, the initial flaw size is a 0.10 in. radial corner crack. For reamed fastener holes, the initial flaw size is assumed to be a 0.05 in. radial corner crack. If the fastener hole contains a driven rivet, the initial flaw is a 0.005 in. radius corner flaw. The specification requires that initial damage flaws can be detected with a 90% probability of detection and a 95% confidence level.[3]

NDE methods using penetrants or magnetic particles must be capable of detecting surface flaws of at least 0.075 in. x 0.150 in., or an equivalent area, according to MIL-A-83444.[2] Similarly, the military specification states that ultrasonic inspection should detect embedded flaws of 0.100 inch diameter.

Acoustic emission monitoring has been demonstrated for the measurement of fatigue cracks as small as 20 thousandths of an inch, at tests at Wright Research and Development Center.[4] In other tests of acoustic emission monitoring technology, all cracks with depths greater than 0.3 mm were detected in a Mirage spar by a group at the Aeronautical Research Laboratories in Australia.[5]

The strength and rigidity requirements for repeated loading conditions applicable to Navy procured airplanes are delineated in MIL-A-8867C.[6] For damage tolerance compliance, it specifies an initial flaw size of 0.01" in metals and at failure, not smaller than 0.25" (surface length). MIL-A-8867C contains the requirements which define the ground tests required for structural evaluation of airplanes. It also specifies the inspection frequency of the aircraft (every 250 hours for general inspection, every 1000 hours for major inspection). MIL-1530A describes the Air Force Aircraft Structural Integrity Program and defines the overall requirements necessary to achieve structural integrity of USAF airplanes.[7] It refers to MIL-A-83444 for specifying damage tolerance design requirements.

Acoustic emission was used for the detection of fatigue crack initiation and growth, during structural fatigue tests on an F-15 test aircraft, in a report by Pokorski and Fisher.[8] The study focused on two areas of the aircraft, fuselage center section and the port wing upper surface. The research performed showed that the measurement of the acoustic emission signal arrival times using a fixed threshold may lead to errors. The report highlights the fact that, though basic acoustic emission waveform data can provide essential data to locate cracks, improved sensor sensitivity is needed to utilize it for fatigue damage detection for aircraft structures.

Scala, et al., discuss procedures for eliminating extraneous sources of acoustic emission.[9] The capabilities of additional signal processing for identifying and locating acoustic emission from fatigue crack propagation were evaluated, and semi-adaptive processing of acoustic emission waveforms was proposed as a valuable and reliable method for identifying acoustic emission due to fatigue crack propagation, even in the presence of many spurious sources. In a separate paper, Scala and colleagues highlight the need to use relatively sophisticated acoustic emission systems to distinguish between damage-related and spurious acoustic emission sources during the fatigue testing of aircraft components.[10] Different techniques

such as sensor arrays for source location and the use of guard sensors, assist in allowing the identification of damage-related acoustic emission sources.

With regard to detection of delaminations in composite structures, Schmidt, et. al, demonstrated a method for delamination detection within a composite panel using embedded extrinsic Fabry-Perot interferometer (EFPI) sensors. An ultrasonic pulse is used to probe the composite panel.[11] The experimental results show that the ultrasonic pulse is interrupted by the delamination, thus indicating the existence of the delamination. Mast and colleagues at the Naval Research Laboratory modeled the mechanical behavior of composite materials in order to quantify the failure behavior and internal damage of a broad class of composite materials.[12] It postulates an energy density dissipation function as a property of the material. The volume integral of this function is equal to the energy dissipated during loading and its value at any point in the material is regarded as a measure of the load-induced damage. A general theory for the derivation of the constitutive behavior of the damaged composites is also presented.

Corrosion may be classified according to the depth of pits generated by the corrosion process.[13] Light corrosion is characterized by discoloration and/or pitting to a maximum depth of 0.001 inch. If blistering, scaling, or flaking is present, with pitting depths up to 0.010 inch, then the process is characterized as moderate corrosion. When pitting depths exceeding 0.010 inch, or blistering exfoliation is present, the corrosion is categorized as severe.

3.2 Impact Location Using Optical Fiber Sensors and Neural Networks

An investigation was initiated in the use of neural networks to determine impact location by processing the output of a network of fiberoptic strain sensors distributed on a surface. This approach extends the results of Gunther, et al, who showed that impact location by triangulation could be used by comparing the arrival times of the acoustic signal at several sensors.[14] For this study, a commercially available neural network simulator running on a personal computer was used to train a network using a back-propagation algorithm. The ability of the network to determine impact location by time-of-arrival of acoustic signals was assessed by comparing network outputs with actual experimental results using impacts on a panel instrumented with optical fiber sensors.

3.2.1 Development of Impact Detection and Location System Using Adaptive Neural Networks

The method we used to detect surface impacts involved analyzing the propagation of acoustic surface waves produced by the impact. Namely, the time-of-flight differences of these waves were examined between several sensor points on the impacted surface. One method of calculating the location of an impact using these time differences is triangulation. However, we utilized an adaptive neural network to analyze these time differences and calculate the location of the impact. An overview of neural networks follows.

Neural networks are structured much in the same way the human brain is structured. Unlike a conventional computer program which consists of one central processing unit performing a rigid set of instructions on given inputs, a neural network consists of many smaller processing elements (PEs) or neurons which are all interconnected. The connections between the PEs are made stronger or weaker as the network is trained, thus affecting the output. Training involves giving the network a series of typical inputs along with the known desired outputs. After processing the inputs once, the neural network calculates the RMS error between the actual output and the desired output. Adjustments are then fed back to the connection weights so as to minimize this error on the next training run; the same input set is then repeatedly used until the weights for each connection have been sufficiently modified to minimize the error. This type of network is called the back propagation network, since information concerning the error flows opposite to the flow of processing information. After the RMS error has been sufficiently minimized through repeated training, the network can be tested. The only difference between training and testing is that the connection weights are not adjusted after each input is processed.

To ensure that this method of impact detection was feasible using a neural network, the net was tested using a set of hypothetical impact locations generated using the computer application Mathematica™. The coordinates for the impact locations were randomly generated, and uniformly distributed across the hypothetical surface. From these, the time-of-flight differences were calculated using

$$\Delta t_{12} = \frac{\sqrt{(x_1-x_0)^2+(y_1-y_0)^2} - \sqrt{(x_2-x_0)^2+(y_2-y_0)^2}}{v}, \qquad (1)$$

where (x_0,y_0) are the Cartesian coordinates of the impact, (x_1,y_1) and (x_2,y_2) are those of the first and second sensor, respectively, and v is the velocity of the surface wave in the material. Here, the assumption has been made that the material impacted is acoustically isotropic. The values used corresponded to what was used during some of the actual tests, that is, a 1m x 0.5m sheet of aluminum.

These results were then fed into a back propagation network, using the Δt's as input, and the impact coordinates as output. The best results after 50,000 simulated impacts were an average error of 0.462 cm in the x-direction , and 0.220 cm in the y-direction. From this we concluded that the neural network should work well in detecting actual impacts.

To help generate the impacts in an actual laboratory test, an impact table was constructed, as shown in Figure 3.2-1. The table allows the implementation of impacts which are very repeatable, and which can be located quickly using calibrated centimeter rulers (not shown) on the top surfaces of the guide rails. The PVC tubing is free to move on the support rods, to position the plumb bob above the desired impact location. The impact is created by bouncing the plumb bob off the surface of the table, using the nylon cord to lift the weight. The wing nuts can be tightened to help eliminate extraneous rattling, which might generate unwanted sensor noise; the rubber insulation between the panel and the frame should also act to alleviate this noise. The sensors are placed in each corner, with their axes along the diagonals of the sheet of aluminum. This placement helps to ensure that the maximum amount of disturbance energy is incident on the sensor. Since the time-of-flight differences are to be calculated using the first major disturbances seen by the sensors, reflections from the edges of the panel are not expected to be a problem.

3.2.2 Impact Detection and Location Test Results

We successfully implemented a back propagation neural network to perform impact detection on both isotropic and anisotropic materials, by post-processing data from extrinsic Fabry-Perot interferometer (EFPI) sensors functioning as acoustic sensors. Two sets of experiments were performed, first on a 100 cm x 50 cm x 3 mm aluminum panel, then on a 38 cm x 44 cm x 4 mm carbon fiber polymer matrix composite panel with 12 plies. In the aluminum panel case, an EFPI sensor was surface mounted in each of the four corners of the plate. The composite panel was made with a sensor embedded in each corner. One sensor failed to survive the composite panel fabrication process and had to be replaced with a surface mounted EFPI sensor. Overviews of each test are given below, along with the results and complications for each one. Suggestions for improvements are given in Section 3.2.3.

3.2.2.1 Acquiring Experimental Data

The data that were collected in both the aluminum and composite panel tests were the differences in arrival times of the stress wave signals between sensors. All data were read using cursor placements on a digital sampling oscilloscope, which was triggered on the first acoustic event detected by any sensor. One difficulty was deciding where to place the cursors on the oscilloscope; impact location could be

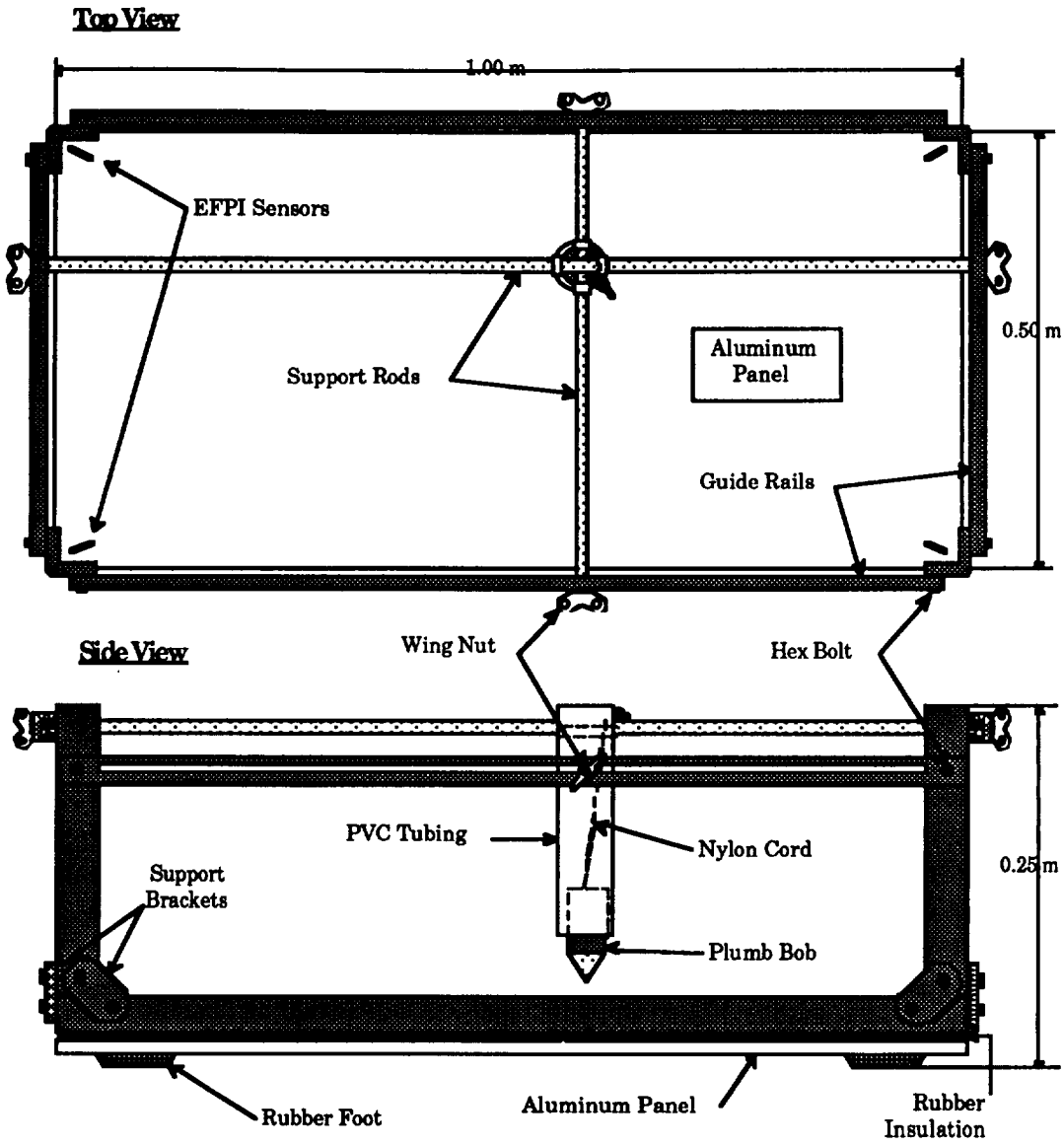

Figure 3.2-1. Impact generation table

performed using two different measurement schemes, depending on where the cursor was placed. The reference could be taken as the first threshold of an event above the noise floor of the oscilloscope trace; alternately, the peak sensor output for a given trace could be used. The best results were obtained using the first threshold event, due to sensor quiescent point instability which caused ambiguous output; in some cases, the maximum strain on the sensor did not register as the peak output on the oscilloscope, due to a turn-around point in the sinusoidal sensor output.

3.2.2.2 Neural Network Improvements

An enhanced and upgraded version of the neural network simulation software (NeuralWorks Professional II Plus) was later installed, giving us the ability to evaluate networks with more than four inputs. The software also allowed us to alternate training and testing of a network, which avoided over-training a back propagation network. Over-training occurs when the network becomes too specialized to the current training set, and no longer tests well with data points outside the training set. By examining many different combinations of training and testing sets, the average error for impact location was eventually decreased using this "Save Best" utility.

3.2.2.3 Aluminum Panel Tests

Three sets of impact data were acquired, the first consisting of 37 impact points, and the second and third consisting of 35 impact points. The first and third sets were acquired using the first-threshold cursor method, and the second using the peak sensor output cursor method. The values that were read off of the oscilloscope were the time differences between sensor 1 and sensors 2,3, and 4 (yielding Δt_{12}, Δt_{13}, and Δt_{14}). The other three time differences, Δt_{23}, Δt_{24}, and Δt_{34} were simply calculated from the other three ($\Delta t_{23} = \Delta t_{13} - \Delta t_{12}$, etc.). These six time differences were the inputs into the back propagation neural network. Although these additional three calculated time differences might seem to be redundant, it was found that the accuracy of the neural network improved when this redundancy was introduced, i.e. when the number of inputs increased from three to six. The outputs were the x and y coordinates of the impact, and these were also input to the network during training.

The back propagation neural network that was used consisted of one input layer, with six processing elements (PEs), one hidden layer with three PEs, and one output layer with two PEs. This architecture was developed through trial-and-error, based on minimizing the average error over all test points. Next, the "Save Best" utility was implemented, which trained the network for one full training set, and then tested the network. The root-mean-square (RMS) error was calculated for each test and compared to the result obtained in the previous test; if there was a reduction in the RMS error, the network weights were saved, and the training/testing process was repeated. The entire process stopped when there was no improvement after 500 successive tests.

The initial approach to training a neural network was to separate a few points from each main data set to be used to test the effectiveness of a trained network. For the first set, thirty points were used to train the neural network, and seven were used to test it after training. Five points were used to test the second and third sets, still

using thirty to train. It was later discovered, mostly from trial and error, that a network's success in locating an impact was very much dependent on which points were removed from the data set to be used for testing. This is most likely due to "outlier" points within the data set being used to test the network. Therefore, we adopted a method for finding an average impact location error for a given neural network, by training and testing with many different combinations of points. The method used is as follows:

- The data set was "shuffled" by row, i.e. the order of impact point location was randomized.
- The last seven (five) points were taken as the testing set, the remaining thirty as the training set.
- A neural network was trained and tested using these sets.
- The above three steps were repeated nine more times, resulting in ten impact location neural networks, each with a different impact location error.

The average location error for the x and y directions was calculated between the ten sets, along with the standard deviation. The results are summarized below for all three sets of data, in Tables 3.2-1 and 3.2-2.

As can be seen from these tables, the best results were obtained from the third set of data; this was probably due to the experience gained in performing data acquisition for the first two tests. The relatively high error over all three data sets can be attributed to two factors. First, there was some ambiguity in reading oscilloscope traces, caused by low sensor response to acoustic events. This is well illustrated in the oscilloscope traces shown in Figure 3.2-2. The first sensor event on the trace corresponding to sensor #3 is relatively easy to distinguish, whereas the first event is almost non-existent with sensor #2, even with a voltage resolution which is ten times greater.

The low number of points (30) used to train the network was also a factor, since it was determined that this hinders the performance of back propagation networks. Still, these results seemed promising enough to continue on, and attempt to perform impact location on a composite panel, provided more impact data points were taken.

	Set #1, x	Set #1, y	Set #2, x	Set #2, y	Set #3, x	Set #3, y
Network #1	5.8241	4.5960	5.3152	3.2709	3.0917	1.4675
Network #2	5.9565	2.5280	6.5489	3.9976	5.5931	4.2319
Network #3	5.3635	5.9792	10.3528	5.7217	3.5932	3.6433
Network #4	5.4796	4.7323	2.8128	1.5864	9.7945	2.9253
Network #5	6.7333	7.4655	3.5852	2.3397	7.3191	4.3277
Network #6	6.7732	3.7795	4.8229	4.4307	4.0657	2.5038
Network #7	7.5709	7.4054	11.5727	5.7512	6.8966	3.9695
Network #8	6.2973	3.5255	4.8349	6.0433	3.7331	3.8300
Network #9	5.7513	6.5539	5.0883	3.6834	5.0862	2.9947
Network #10	7.1296	5.3958	6.7818	2.0366	3.1413	4.4062

Table 3.2-1: Average error in locating an impact (aluminum panel), in centimeters

	Set 1, mean	Set 1, St.Dev.	Set 2, mean	Set 2, St.Dev.	Set 3, mean	Set 3, St.Dev.
x-direction	6.2879	0.7385	6.1716	2.8018	5.2314	2.1944
y-direction	5.1961	1.6673	3.8862	1.6100	3.4300	0.9458

Table 3.2-2: Statistical data for Table 1 averages, in centimeters

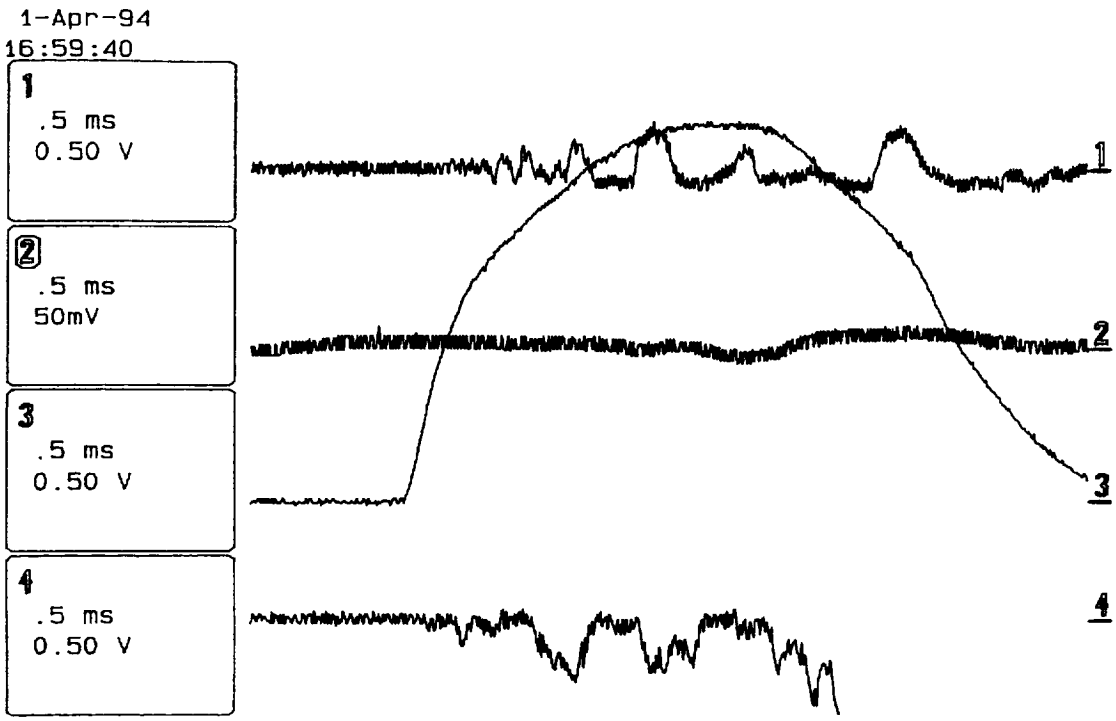

Figure 3.2-2. Example of ambiguous oscilloscope trace

3.2.2.4 Composite Panel Tests

A graphite/bismaleimide composite coupon measuring 38 cm x 44 cm x 4 mm was fabricated in the Composite Fabrication Lab at Virginia Tech. The panel consisted of twelve plies, all with the carbon fibers running along the longer dimension. This lay up was chosen to result in a panel with a high degree of anisotropy with respect to the acoustic velocity. The EFPI sensors were embedded close to the surface, between the third and fourth plies, oriented along the diagonals of panel. After processing the panel through the hot press and testing the sensors, one sensor (#4) was found to have failed, and a surface-mounted EFPI sensor took its place. It should also be noted that sensor #3 would display output behavior both when the panel was impacted, and when the lead-in fiber was perturbed; neither sensors #1 nor #2 behaved this way. This undesirable response was probably caused by a crack in the lead-in fiber to the sensor, which gave spurious signals. The test was still performed using this sensor, since this was not thought to affect the neural network's ability to locate impacts; because the method of impact location was utilizing the first acoustic event to the sensor, any disturbances to the lead-in fiber which may have caused the undesirable signals would have occurred after this first acoustic event.

Only one test was run on the panel, but many more impact points were performed. The entire set comprised 132 impacts, with 120 being used for training, and twelve for testing. The same method of randomizing the data set that was performed for the aluminum panel was done with this data set. A similar summary is given below in Tables 3.2-3 and -4. The results for the composite panel were much better than the aluminum panel tests. The principal reason is believed to be the increased number of impacts used to train the neural network. The results were quite good, even though inspection of the data showed that the time difference between sensors

	x	y
Network #1	1.5335	1.9067
Network #2	2.2557	3.1391
Network #3	2.4581	3.4098
Network #4	2.6825	3.2009
Network #5	3.2982	3.0912
Network #6	2.0625	3.2832
Network #7	2.3067	2.2919
Network #8	1.0063	3.2216
Network #9	2.0576	2.8142
Network #10	1.9576	5.6149

Table 3.2-3: Average error in locating an impact (composite panel), in centimeters

	Mean	**St.Dev.**
x-direction	2.1619	0.6211
y-direction	3.1973	0.9744

Table 3.2-4: Statistical data for Table 3 averages, in centimeters

one and three (Δt_{13}) was inconsistent with expected results; this then opposes the initial assumption that sensor #3 would work well even with a cracked lead-in fiber.

An attempt was made to improve the aforementioned results, first by eliminating the edge impacts (impacts near the edge of the panel). By inspecting the time differences, we discovered that the values for edge impacts were inconsistent, which presumably created an ill posed data set to the neural network. This inconsistency is illustrated below in Figure 3.2-3, where the x and y axes represent the x and y coordinates of the panel, and the z axis represents the time difference between sensor #1 and sensor #4. Theoretically, the mesh plot should be a flat plane, tilted with its highest corner over sensor #1, and its lowest corner over sensor #4. Here, the surface behaves mostly in this fashion, except for the boundary points. This is why the impact performance was expected to improve when these edge points were removed from the training set.

We also attempted to eliminate the time differences involving sensor #3 (Δt_{13}, Δt_{23}, and Δt_{34}), since the corresponding data was flawed. Impact location would therefore have to be done using only three sensors, and three time differences. In both the edge impact elimination case and the sensor #3 elimination case, there was an increase in impact detection error. This increase in error is attributed to the reduction in the overall number of impact points used to train the network, which was the same problem encountered with the aluminum panel tests.

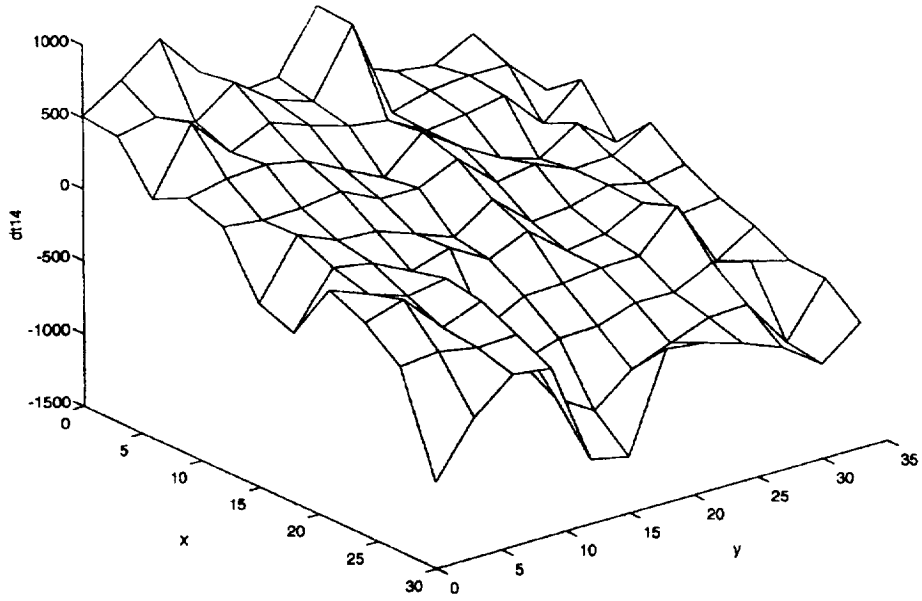

Figure 3.2-3. Three dimensional mesh plot of Δt_{14} (sensor #1 at (0,0), sensor #2 at (0,30), sensor #4 at (30,35))

3.2.2.5 The Dual-Wave Phenomenon

Although the aforementioned results are promising, an interesting phenomenon was observed while acquiring the data. The outputs of the sensors indicated that the direction (compression vs. tension) of the first strain detected depended on the distance of the sensor from the impact. This is illustrated below in Figure 3.2-4; the first plot (Figure 3.2-4a) is a representation of a typical sensor output when the impact point is very close to the sensor. The second plot (Figure 3.2-4b) is representative of an impact point relatively far away from the sensor.

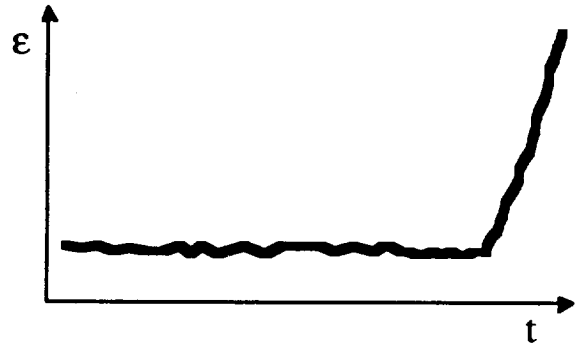

Figure 3.2-4a: Typical near impact

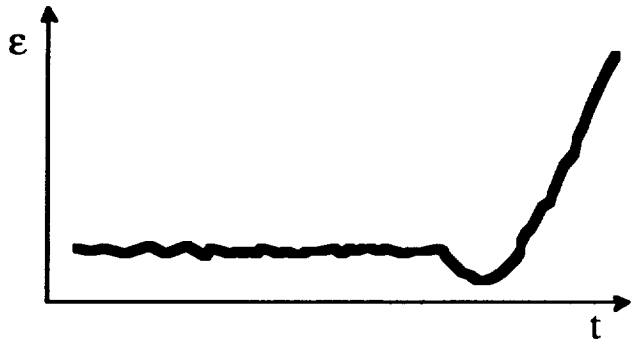

Figure 3.2-4b: Typical far impact

This reversal of the initial direction of the output trace corresponds to a sensor experiencing one type of disturbance (either tension or compression) when the impact is near the sensor, and a different type far away from the sensor. This led us to the conclusion that the impact was exciting two different types of acoustic waves within the composite panel. The fact that different sensor responses were recorded with different impact distances implies that the two waves have different velocities. To test this hypothesis, an EFPI sensor was surface mounted at the center of the panel to trigger the oscilloscope. The panel was impacted very close to this sensor, while a PZT piezoelectric transducer was used near the edges of the panel to monitor acoustic waves. Three examples of the results are included.

The first example (figure 3.2-5) reflects a transducer placement such that the acoustic waves are propagating perpendicular to the composite fibers, the second (figure 3.2-6) example reflects sensor placement for acoustic waves traveling at 45° to the fibers, and the third (figure 3.2-7), parallel to the carbon fibers. There are two things that should be noted from these traces: (1) there are two waves present, a smaller one preceding a larger, more prominent wave, and (2) the time difference between these two waves decreases as the sensor moves from perpendicular to parallel to the composite fibers. In all three cases, the distance between the impact point and the transducer is approximately the same. This data supports the theory that there are

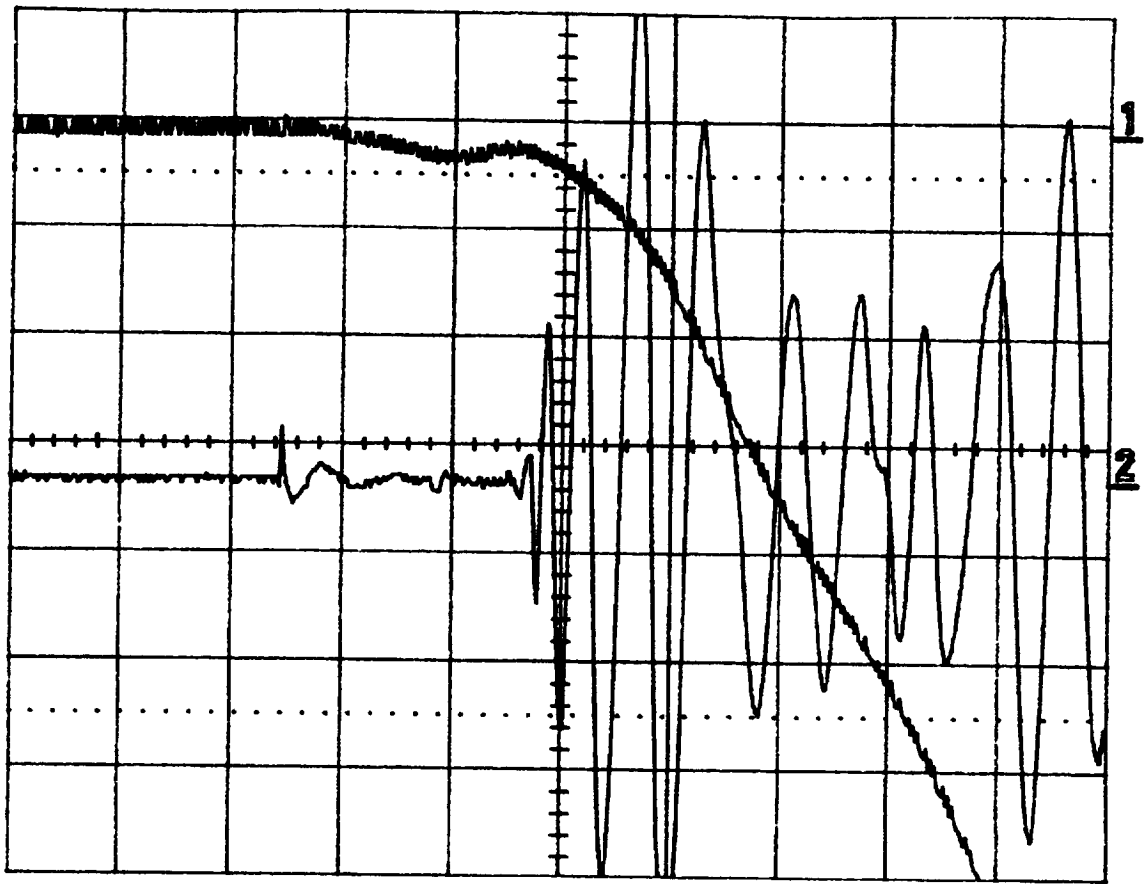

Figure 3.2-5. Acoustic wave perpendicular to composite fibers
(Trace 1 is the output of the EFPI sensor used as a trigger,
and Trace 2 is the output of the PZT transducer)

two types of waves present in the composite panel. Further tests have shown that the smaller wave is more prominent when the panel is impacted edge-on, instead of on the surface, suggesting that the smaller wave is longitudinal in nature. The sensor output for the longitudinal wave is smaller than the second wave, because the impact generates predominantly flexural waves, and the longitudinal wave is stimulated through the Poisson effect. It is likely that the larger wave is the flexural waves. This interpretation is consistent with the fact that in most materials, the speed of longitudinal waves exceeds that of flexural waves. Their effect on impact location has yet to be determined.

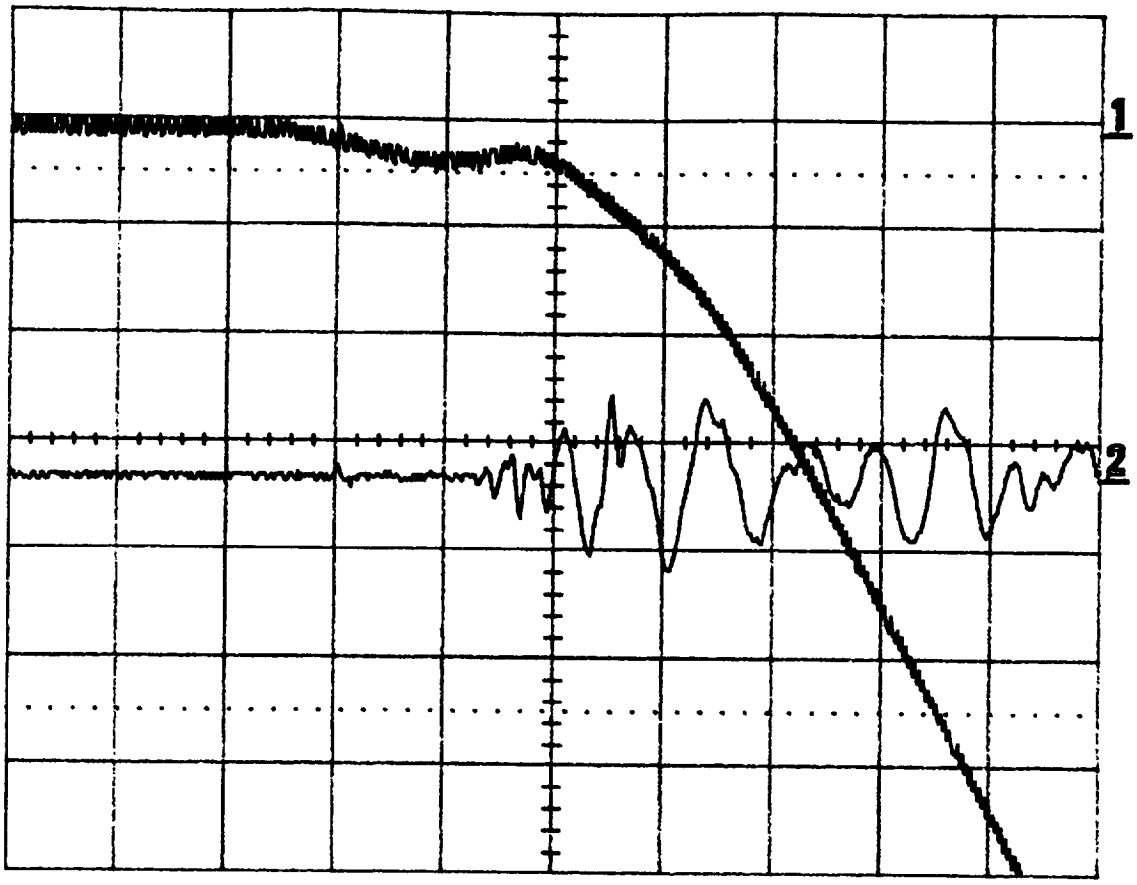

Figure 3.2-6. Acoustic wave 45° to composite fibers.
(Trace 1 is the output of the EFPI sensor used as a trigger,
and Trace 2 is the output of the PZT transducer)

3.2.3 Discussion of Results

Since the end results of this research are to be applied to aircraft which most often are made up of curved, not flat surfaces, this aspect must be addressed. One advantage of using neural networks with time-of-flight impact detection is that detection is independent of the shape of the object, as long as the material is isotropic. Some ideas have been to use a cone, or half-sphere for subsequent tests.

If this impact detection system is eventually to be applied over a large surface, such as an aircraft wing, some determination will have to be made as to how many sensors will be needed for a given surface area. This will depend on the sensitivity of the sensors, and the ability of the neural network to pinpoint an impact. Another aspect that would have to be determined is how much accuracy is needed for a given application.

Currently, location of the impact is to be done using post-processing methods; after determining the time differences, the numbers are input into a separate computer, where the neural network will give the impact location. Later, possibly with the help of a computer system such as LabView, *in-situ* processing should be used to locate an impact directly after it occurs. Eventually, some kind of "black box" would have to be developed to perform the calculations to determine the time differences, and download these to a neural network, either one centrally located on the aircraft, or many dispersed in a modular fashion.

There is still some question as to how much internal composite structure damage is being caused by performing these impact tests, and how any internal damage would affect a neural network's performance. The effect of composite damage on neural network performance could be evaluated by training a neural network to locate impacts on a particular panel, and then subject the panel to stress that is likely to introduce internal damage, cracking, or delamination. Then, the same neural

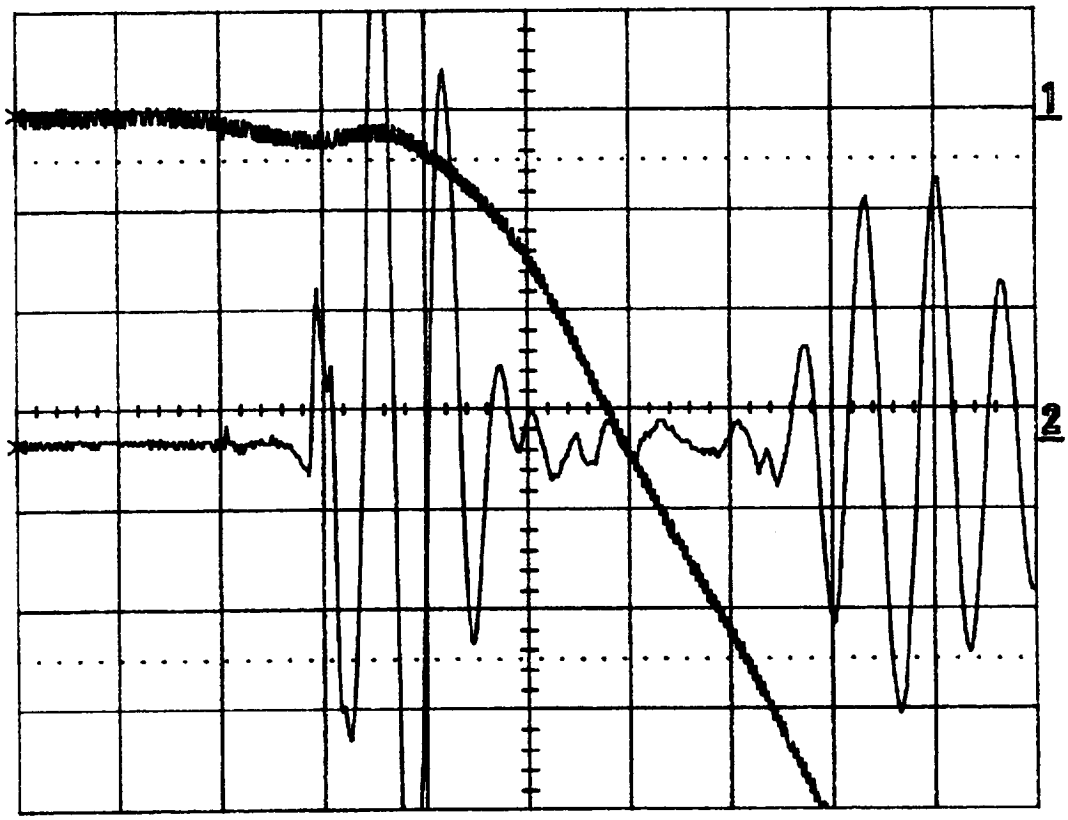

Figure 3.2-7. Acoustic wave parallel to composite fibers.
(Trace 1 is the output of the EFPI sensor used as a trigger,
and Trace 2 is the output of the PZT transducer)

network would be used to locate impacts on the damaged panel, and a comparison of its ability to locate impacts before and after damaging could be done.

One aspect of fatigue cracks that has not been addressed yet is crack detection through acoustic emissions. Whether or not this is a feasible approach will be determined by the sensitivity of the fiber sensors to this phenomenon, and also by the ability to filter out spurious noise sources, which are invariably present with this application.

3.3 Optical Fiber-Based Corrosion Sensors

Research into the use of optical fiber sensors for the detection of corrosion in metals was undertaken in the second year of this research grant. Specifically, we evaluated metal coated fibers with long-period Bragg gratings, and EFPI strain sensors with plastically deformed metal coatings.

3.3.1. Conventional Corrosion Detection Methods

Many different methods exist to monitor corrosion, from simple visual inspection, to state-of-the-art quantitative sensing methods. In the commercial airline industry, the most popular (and not surprisingly, the least expensive) method for determining corrosion damage is visual inspection.[15] Visual inspection can be characterized as simply the examination of a part for pitting, cracking, discoloration, and/or flaking and bubbling of paint or coatings. The principal flaw of visual inspection, though, is that it is essentially subjective in attempting to quantify the amount of corrosion damage. In some cases, this could provide misleading conclusions. With some types of bridges, a layer of rust helps protect the structure from further corrosion damage, since the corrosion by-product is atmospherically inert. On the other hand, a metal composite material might be unblemished on the surface to visual inspection, while the underlying metal layers are severely weakened from corrosion damage. Also, in the case of most aircraft, areas which are especially sensitive to corrosion damage or critical to the overall structure of the aircraft are not very accommodating to visual inspection; the aircraft must be removed from service and disassembled to reach these vital areas.[16] Instruments such as fiberscopes can be employed in this case, but they are difficult to manipulate in small closed areas, and the image reproduction can sometimes be misleading. Other methods that are used to detect corrosion include electrochemical and electromagnetic sensing, some of which are summarized below.

Since corrosion is both chemical and electrical in nature, certain electrical methods can be utilized to measure its onset. Essentially, corrosion can be envisioned as an electrical circuit, typically modeled by the galvanic cell; the most simple example of a practical galvanic cell is the power production in a battery. Oxidation, or loss of

electrons, occurs at the anode of the system, while reduction, or gain of electrons, occurs at the cathode of the system; metal loss occurs at the anode during corrosion, metal gain occurs (in some cases) at the cathode. There can be physical contact between the anode and cathode, or they can be separated by an electrolyte. In both cases, the circuit must be closed for corrosion to take place. In the case of an iron nail in salt water, the cathode and anode take the form of macromolecules of iron which are distributed over the entire surface area of the nail; hence, rust forms uniformly over the surface.[17] Similar to examining the potential, current, and resistivity of a simple battery, these methods can be applied to examine corrosion. Tests can be performed under controlled potential conditions, controlled current conditions, and at AC frequencies to measure impedance.[18] With some special modifications, a simple galvanic cell can be used as a corrosion coulometer, which measures the ambient corrosion of steel, taking into account debris accumulation (essentially corrosion products) and airborne contaminants.[19]

X-ray diffraction, a type of thin-film analysis, can be performed to interrogate corrosion, analyzing surface composition and morphology. The surface being interrogated is usually an oxide layer which has formed following exposure to a corrosive medium. X-rays incident on the surface of the specimen scatter according to oxide chemistry, grain size, thickness, and lattice parameters and orientation. For the method to be effective, certain geometrical requirements must be met, dictated mostly by Bragg's law of diffraction. The sample can be measured directly following corrosion, or first ground into a powder.[17] Electron probe microanalysis is similar to x-ray diffraction in that the corroded sample emits characteristic x-rays when interrogated with high-energy electrons. The difference is that the sample is interrogated over a very small surface area, usually one micron in diameter. This precision gives the test operator the ability to examine very specific areas with greater ease.[17] When elliptically polarized light impinges upon a thin-film surface, the reflected wave will exhibit a change in polarization, which can be correlated to the type and thickness of the thin film. This type of corrosion evaluation is known as ellipsometry. The laws which dictate the reflected wave's characteristic polarization shift are primarily Fresnel's Law and Snell's Law of Refraction.[20] Finally, one novel method for detecting corrosion is a thin-layer activation method for detecting minute losses of material. A section of interest on the sample is radioactivated and calibrated to sensing equipment before corrosion takes place. The change in radioactivity of the active portion is monitored as the thickness is reduced from wear or corrosion. Although the method is very accurate, it is limited to a surface depth of a few hundred microns.[21]

3.3.2. Corrosion Sensors

The variety of corrosion sensors is quite vast; each has its own particular strengths and weaknesses for different applications. Methods for inspecting gas, liquid, and

solid material pipelines for corrosion include the use of weight-loss coupons, electrical resistance tests, zero-resistance ammetry (ZRA or galvanic measurements), hydrogen-permeation, electrochemical-impedance measurements (EIM), and linear-polarization resistance sensors (LPR).[22] Additionally, aqueous corrosion detection has been demonstrated through the development of an electrochemical noise sensor. The sensor consists of a voltage source and a current source, with data being evaluated using power-spectrum analysis. The presence of corrosion corresponds to an increase in the amplitude and number of fluctuations of the voltage and current power-spectrum densities. The results of the tests show that current-noise measurements were found to be more comparable to typical methods of corrosion detection than potential-noise measurements.[23]

The drive towards the miniaturization of sensors has affected corrosion engineering substantially, with the development of many different types of corrosion microsensors, along with the development of microprocessor technology for faster, remote data manipulation and storage. Different kinds of non-optical corrosion microsensors include single-ion redox transducers, chemically sensitive semiconductor devices, galvanic transducers, polarization transducers, and resistance transducers, among others. Laboratory tests have been documented on a three-electrode sensor, a current distribution probe, an electrical resistance probe, and a multiple-element sensor.[24,25] Additional microsensors include surface acoustic wave (SAW) devices, and the quartz crystal microbalance (QCM) device.[26] In many areas, such as manufacturing process control, automated corrosion detection has moved beyond the domain of research, and has become commercialized. Case studies are available in many fields, explaining the merits and faults behind such systems as the Onguard™ corrosion monitoring system,[27] and automated ultrasonic testing systems, which use ultrasonic technology to examine the corrosion of hidden surfaces. One particular case study delves deeply into the actual method of operation of the particular pieces of equipment used on an oil pipeline in the Arctic.[28] Also used to inspect long-distance pipelines are autonomous robots, or "pigs" as they are known, one of which employs 448 sensors around the entire circumference of the forty-eight inch diameter robot. These sensors are used to detect (among other things) dents, cracks, and corrosion damage, all from the inside of the pipeline.[29]

3.3.2.1 Optical Sensor Methods for Corrosion Detection

The use of optical sensors and fiber optic sensors is quite new in the corrosion detection arena; their popularity has grown recently due to advances in materials and sensing research. Fiber optic sensors have the advantage of small size, low weight, and an inherent immunity to electromagnetic interference. Potentially,

they may be multiplexed with other fiber optic sensors, as well as with optical communication systems.

One method for detecting the corrosion of metals utilizes a plasmon fiber optic sensor. The theory centers around the premise that, as polarized light propagates through the core of a single mode fiber coated with a thin film of metal, energy is coupled into the metal in the form of surface plasmons, which then changes the intensity of the light exiting the fiber. As the thickness of metal is reduced due to corrosion, the number of surface plasmons is reduced, which is sensed as an increase in intensity[30,31]. While this sensor has shown that it can monitor corrosion, it is somewhat difficult to manufacture, since metal coatings must be applied to the core of the fiber, a relatively delicate process.

Other simpler and less accurate intensity-based methods use unpolarized light, and metal coatings on multi-mode fiber; intensity differences are simply a function of how much interference is created by the metal coatings. Another fiber optic method of corrosion detection is the "micromirror" sensor; an optical fiber is coated at one end with a chemically sensitive substance whose index of refraction changes when subjected to corrosion, changing the behavior of the reflected signal.[25] Other optical methods include using holographic interferometry, thermography, and evanescent wave absorption spectroscopy. In holographic interferometry, a transmission hologram is taken of the specimen before corrosion takes place. The subsequent decrease in thickness is seen through the original hologram as an increase in the number of interference fringes. The technique is quite accurate, but very susceptible to changes in material microstructure and position, causing an insurmountable decrease in fringe contrast.[32]

Since most types of paints used to protect sheet metals from corrosion are transparent to infrared radiation in the 3.5 to 5.5 micron range, thermography can be utilized to examine corrosion under a layer of paint. To work effectively, the test samples are regulated at an elevated temperature and must exhibit distinct emissive images during corrosion, versus non-corroded specimens. The technique suffers from subjective analysis, however, since determination of corrosion is dependent on comparisons to reference photographs.[33]

A relatively unique method of corrosion detection uses optical fiber Fourier transform infrared (FT-IR) evanescent wave absorption spectroscopy; the sensing method is based on Attenuated Total Reflectance (ATR) spectroscopy. Qualitative tests were performed on powdered samples of aluminum alloy and aluminum hydroxide (the most common by-product of aluminum corrosion). The fiber sensors are extremely sensitive to very small amounts of sample material, demonstrating that the technique merits more quantitative studies.[34]

3.3.2.2 Thick-Film Coated Sensors for Corrosion Detection

Thick film coatings on fiber optic strain sensors have demonstrated the ability to store strain history of extrinsic Fabry-Perot interferometer (EFPI) sensors.[35] Here, the term "thick film coating" is a relative term, used to differentiate it from thin film technology used primarily in the microelectronics field; the coatings used on the all the sensors in this research are between one and fifty microns thick. The theory behind this memory storage revolves around inducing plastic deformation of the metal coating encapsulating the interferometric sensor, and the ability of this plastically deformed metal to hold the sensor in the strained position. Since a reduction in the thickness of the plastically deformed metal would cause the sensor to relax to its pre-strained state, this method of memory retention in metal coated strain sensors would be feasible for corrosion detection.

However, before the sensors can be used for corrosion detection, plastic deformation of the thick metal coating must first be induced. This plastic deformation can be difficult to achieve, since the process of applying a thick coating of metal is quite involved, and achieving plastic deformation of the metal can sometimes cause the sensor to break; with so much time and effort placed on achieving a thick metal coating, breaking the sensor attempting to induce plastic deformation becomes cost prohibitive.

The method would work similarly if the sensor were first strained, and while holding the sensor in this strained position, a sufficient amount of metal was applied to the sensor so as to hold the sensor in the strained position; the metal coating would hence be in a state of compression upon release, assuming there is adequate adhesion between the metal coating and the glass fiber. Then, as the volume of metal is reduced due to corrosion, or the strength of the metal is compromised by corrosion, the sensor would relax back to its original pre-strained position. It is the relaxation over the corrosion lifetime of the sensor that is the sensing mechanism of part of the corrosion sensor design in this study.

The second approach undertaken during this grant involves detection of corrosion in metal coatings on optical fibers with long period Bragg gratings in the fiber core. The long period grating (LPG) optical fiber sensor is a technology that has just recently been developed. The LPG sensor responds to changes in the index of refraction surrounding the sensor. The proposed method of corrosion detection is to coat the sensor with metal and examine its response as the metal corrodes and the ambient index of refraction changes.

3.3.3. Theoretical Development

The method of corrosion detection examined in this portion of the study revolves around the ability of a thick metal coating to hold a fiber optic strain sensor suspended in elastic strain. The theoretical mechanics behind this sensing action are dependent on several requirements; however, these conditions are not always necessary and/or sufficient for corrosion sensing to occur. They include:

- Perfect adhesion at the glass/metal interface
- Uniform corrosion over the surface of the sensor
- Uniform corrosion over the lifetime of the sensor
- Metal coating strain behavior equivalent to bulk metal
- Zero strain on the sensor at zero coating thickness

In actual tests, the aforementioned conditions are subject to practical limitations and other physical laws:

- Adhesion between the glass and metal is dependent on which method is used to apply the initial coating of metal.
- Due to variations in environmental surroundings and conditions, and also sensor surface mounting schemes, corrosion could occur more rapidly on different surfaces of the sensor.
- Uniform corrosion over the lifetime of the sensor is very unlikely, due to the reduction in surface area as the coating thickness decreases.
- The physical constants and strain behavior of the relatively thin metal films used in this study are certainly different than those quoted in technical references for bulk metal.
- Because sensor strength is paramount to its success, it becomes necessary to apply a marginal amount of metal before straining occurs, since sensors with metal coatings tend to be stronger.

Below, the theory concerning the operation of the fiber optic strain sensors will be briefly reviewed, followed by the theoretical derivation of the strain sensing method. Then, a brief outline of the theory behind the LPG sensor and its proposed corrosion monitoring capabilities will be presented.

3.3.3.1. The Extrinsic Fabry-Perot Interferometer (EFPI) Strain Sensor

The extrinsic Fabry-Perot interferometer was initially conceived by Murphy et al.[36] A diagram of the sensor and its support system is shown in Figure 3.3-1. A 1330 nanometer laser diode injects light through single mode silica fiber into a two-by-

two fiber coupler. The transmitted light is split between the output ports of a 2x2 bi-directional coupler, as shown in the figure. The light in the lower leg is lost, since this end is shattered, and placed in index matching gel, and therefore does not reflect light. The light propagating in the other output arm interrogates the sensor element. The input fiber of the sensor is cleaved to maximize the amount of reflection at the glass-air interface. Taking the indices of refraction of glass and air into account, the reflection at this interface is approximately four percent. Hence, the majority of the light propagates across the air gap to the second reflector endface, where another four percent is reflected back across the air gap. The reflections other than the aforementioned ones are negligible due to the low reflectivity of the endfaces, and losses in the air gap. Since the two reflected signals are coherent, they interfere and propagate back through the fiber coupler to the photodiode detector head. The observed intensity at the detector is given by

$$I_{det} = A^2\left[1+\frac{2t\,a}{a+2s\tan[\sin^{-1}(NA)]}\cos\left(\frac{4\pi s}{\lambda}\right)+\left(\frac{t\,a}{a+2s\tan[\sin^{-1}(NA)]}\right)^2\right], \quad (4)$$

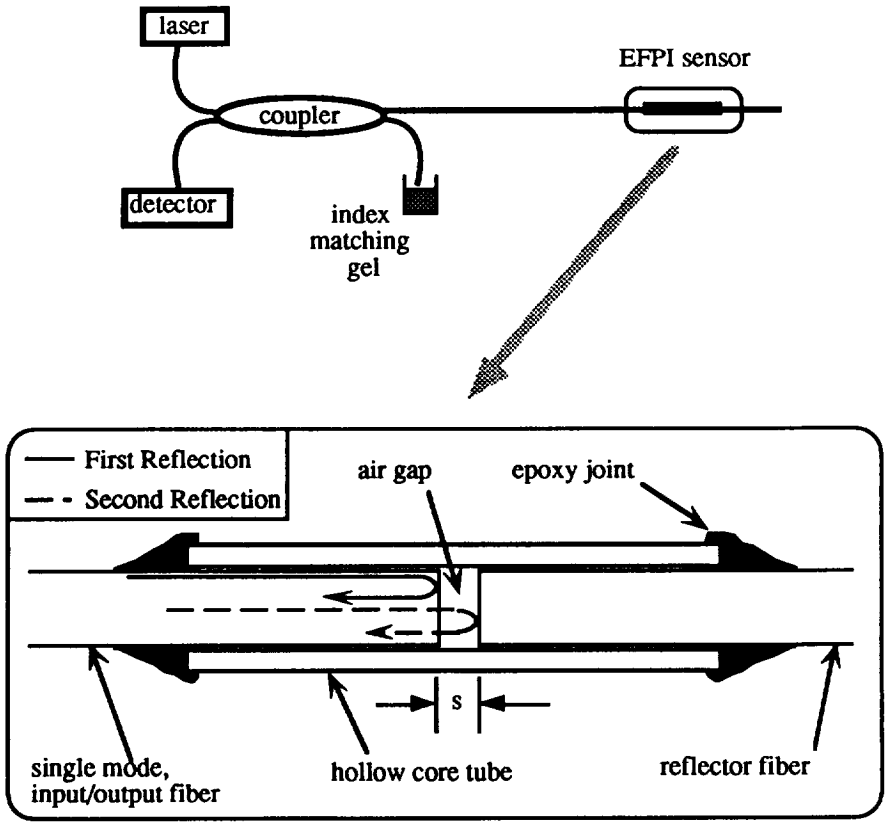

Figure 3.3-1. EFPI sensor system

where A is the amplitude of the first reflection, t is the transmission coefficient of the air-glass interface, a is the fiber core radius, s is the length of the air gap, λ is the wavelength of operation in free space, and NA is the numerical aperture of the single-mode fiber, given by

$$NA = \sqrt{n_1^2 - n_2^2}\,, \tag{2}$$

where n_1 and n_2 are the refractive indices of the core and the cladding, respectively. The type of interference between the two reflected signals depends on the dimension of the EFPI air gap; when the length is an odd integral multiple of $\lambda/4$, destructive interference occurs, and an intensity minimum is detected, and when the length of the air gap is a multiple of $\lambda/2$, constructive interference occurs, causing a maximum in detected intensity. Hence, the detected signal is sinusoidal in nature, as shown in Figure 3.3-2. The exponential decay of the overall magnitude of the waveform is due to the lossy nature of the air gap region.

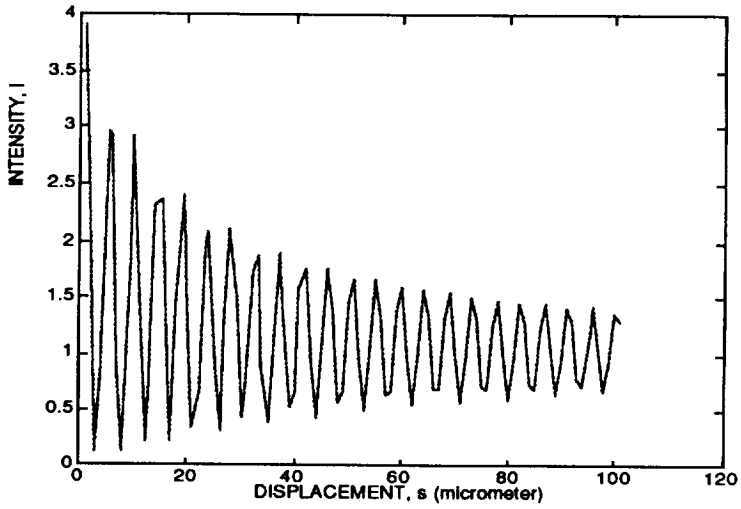

Figure 3.3-2. Theoretical Plot of the Output Intensity (in Arbitrary Units) with Changes in the Air Gap Separation s of an EFPI Sensor.

3.3.3.2. Corrosion Sensing Method Theory

Restated, the method of corrosion detection investigated in this study revolves around the ability of a thick coating of metal to hold residual strain on a fiber optic strain sensor. As the thickness of the metal coating decreases, the residual strain is released. For theoretical analysis of the corrosion detection mechanics,[37,38] the geometry of the EFPI sensor can be simplified as a hollow cylinder of glass, since the sensor architecture used in this study is a sensor design that bonds both the

input/output and reflector fiber arms to the hollow core fiber with epoxy; any stress on the sensor is concentrated on the section of hollow core fiber encasing the two single-mode fiber arms. Assuming that there is perfect adhesion at the metal-glass boundary, it follows that the resulting strains are

$$(\varepsilon_x)_{glass} = (\varepsilon_x)_{metal}, \tag{3}$$

that is, the glass hollow core fiber and the metal coating must share the same amount of strain. The force P exerted on the sensor during perturbation can be expressed as

$$P = \int \sigma_x \cdot dA \tag{4}$$

where σ_x is the axial stress, integrated over the cross-sectional area. The axial stress can be expressed as the strain multiplied by E, the Young's modulus for the material of interest. Hence, for a metal-coated piece of hollow core fiber, the force is expressed as

$$P = \varepsilon \cdot \left[\pi E_g\left(r_2^2 - r_1^2\right) + \pi E_m\left(r_3^2 - r_2^2\right)\right] \tag{5}$$

where r_1, r_2, and r_3 are defined as shown in Figure 3.3-3. To simplify these equations, the cross-sectional areas for the hollow core fiber and metal coating are denoted as A_g and A_m, respectively, so that equation (7) reduces to

$$P = \varepsilon \cdot (E_g A_g + E_m A_m), \tag{6}$$

or, solving for the strain,

$$\varepsilon = \frac{P}{\left(E_g A_g + E_m A_m\right)}. \tag{7}$$

Since the assumption holds that there is perfect adhesion between the glass hollow core fiber and the metal coating, and that the strain is constant across the entire length of the hollow core fiber, the strain in each must be the same at all times. This can be expressed as

$$\varepsilon = \frac{P_g}{E_g A_g} = \frac{P_m}{E_m A_m} = \frac{\delta s_{in}}{L} \tag{8}$$

Also shown in equation (8) is the strain equation for the EFPI sensors, where δs is the change in the air gap dimension, and L is the gauge length of the sensor, or the distance between the two epoxy points. Keeping in mind that the sensor is first

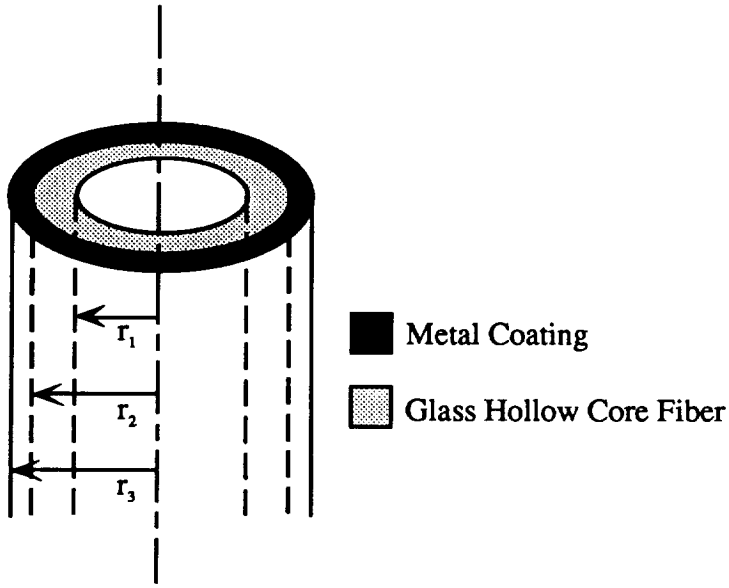

Figure 3.3-3. Cross-sectional dimensions of metal coated hollow core fiber

strained without the metal coating, then the metal is applied, and the strain is then released, the input force before coating can be expressed as

$$P = A_g E_g \cdot \frac{\delta s_{in}}{L}. \tag{9}$$

The sensor gauge length L remains constant throughout the coating and corroding steps, since all of the hollow core fiber is assumed to be coated with metal; the change in air gap before coating is denoted as δs_{in}. Hence, the force on the glass and metal regions are expressed respectively as

$$P_g = \frac{A_g E_g P}{A_g E_g + A_m E_m}, \tag{10}$$

and

$$P_m = \frac{A_m E_m P}{A_g E_g + A_m E_m}. \tag{11}$$

Since the sensor exhibits compressive force instead of tensile force upon release of the stress, the change in the dimension of the sensor's air gap is actually negative; hence, the value for δs_{out} can be conceived as the amount of relaxation upon release of the sensor after applying the metal coating, and is expressed as

$$\delta s_{out} = \frac{P_g L}{A_g E_g} = \frac{P_m L}{A_m E_m}. \qquad (12)$$

Using equations (9) through (12), a plot of stored residual strain and change in gap dimension versus metal coating thickness in an EFPI sensor is shown in Figure 3.3-4 for three different values of δs_{in}. These theoretical curves were derived using a program written in MATLAB®, for several different hollow core fiber pre-strain conditions. The conclusion drawn from this theoretical study is that, assuming there is good adhesion between the hollow core fiber of the sensor and the metal coating, the residual strain release should be sufficient for sensing purposes when the coating thickness is greater than about twenty microns. A comparison of the theoretical models and experimental data is illustrated in Section 3.3.4.10.

3.3.3.3. Long Period Grating Fiber Optic Sensors

When an optical fiber is doped with germanium, it becomes photosensitive; when this germanium doped fiber is exposed to ultraviolet light, there is a change in the index of refraction of the exposed region. When germanium atoms bond with silicon atoms in optical glass (SiO_2), the germanium becomes oxygen-deficient. It is the germanium-oxygen deficiency centers (GODC's) that cause the change in the index of refraction of the UV-exposed glass. The number of GODC's can be increased by hydrogen- or deuterium-loading the fiber, and subsequently making the silica fiber more photosensitive. By constructing optical fiber with a germanium doped core, and exposing the fiber to 244 nanometer plane-wave light through a mask as shown in Figure 3.3-5, a periodic change in the index of refraction in the core of the optical fiber is generated, known as a Bragg grating.[39] For a short period grating sensor, the grating periodicity must satisfy the phase matching condition as defined by

$$\Delta\beta = \beta_1 - \beta_2 = \frac{2\pi}{\Lambda}, \qquad (13)$$

where β_1 and β_2 are the propagation constants of the fundamental LP_{01} mode, and the reverse fundamental $-LP_{01}$ mode (in the other direction along the fiber), respectively. Keeping in mind that

$$\beta = \frac{2\pi n}{\lambda}, \qquad (14)$$

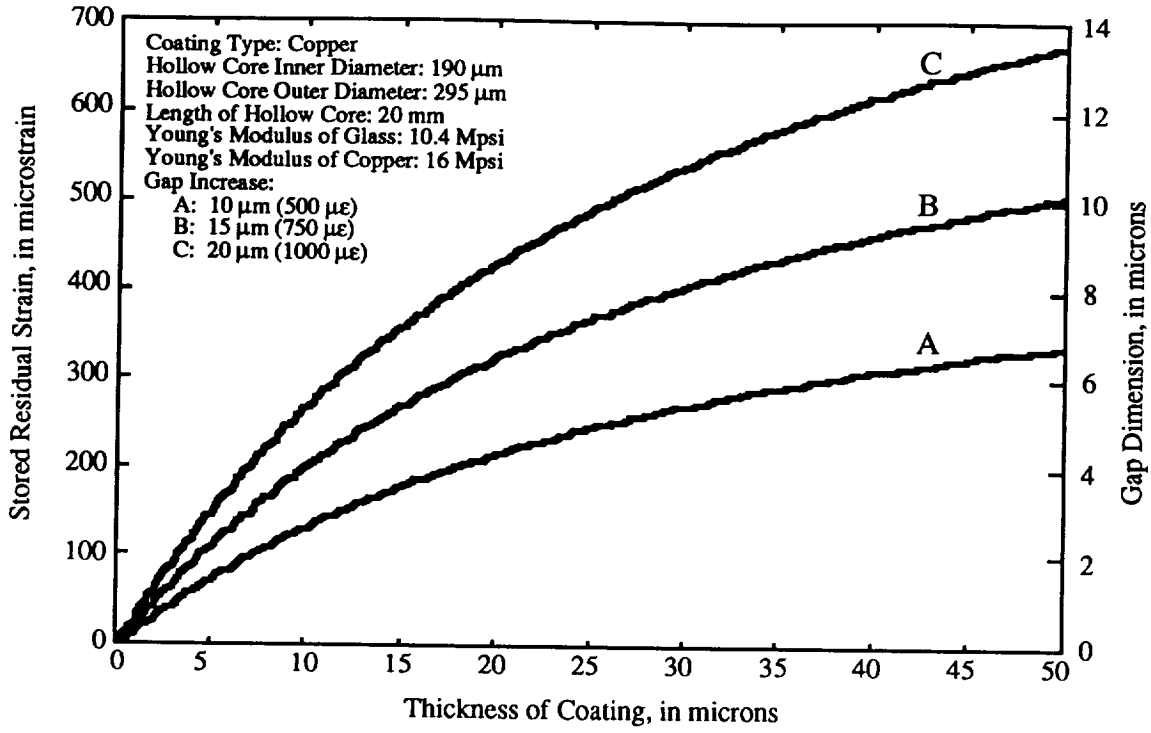

Figure 3.3-4. Theoretical analysis of corrosion sensing technique.

where n is the effective mode index, equation (13) reduces and rearranges to

$$\lambda_R = 2n \cdot \Lambda , \tag{15}$$

where λ_R is the particular wavelength that is reflected from the short period grating. Now consider Figure 3.3-6, which depicts the different propagation constants of discrete core and cladding modes for a single-mode fiber. The fundamental mode LP_{01} and reverse fundamental mode $-LP_{01}$ have a large propagation constant separation, or $\Delta\beta$, and therefore from equation (15), a short grating period. A long period grating would consequently exhibit a smaller $\Delta\beta$; instead of coupling light into the reverse fundamental mode, light would be coupled into the cladding modes, either in the forward or reverse direction. Since both guided and cladding modes possess discrete propagation constants, a highly wavelength-selective device is obtained. Table 3.3-1 has been included to outline the major differences between short and long period gratings.

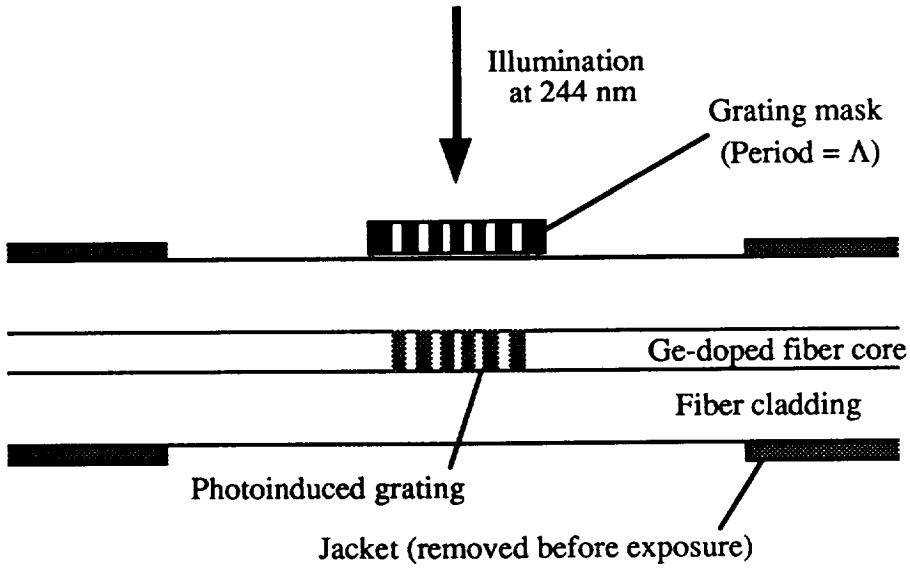

Figure 3.3-5. Long period grating sensor fabrication.

3.3.3.4. LPG for corrosion sensing

Because long period gratings exhibit negligible back reflections, they are especially attractive in the field of telecommunications. Since it is inherently easier to record longer period gratings, and no advantage is attained from coupling to the reverse cladding modes versus the forward cladding modes, LPG fiber optic sensors are fabricated to couple wavelengths to the forward cladding modes, as shown in Figure 3.3-6. When these wavelengths become coupled into the cladding modes, they are severely attenuated, due to fiber bending and jacket losses; as a result, an LPG fiber sensor behaves as a wavelength-selective bandstop filter. Because the spectral location of the attenuation bands is dependent on the cladding of the fiber, any index of refraction changes made to the cladding or jacket regions causes a shift in the attenuated wavelengths.[40] This wavelength shift is the basis of the sensing

Table 3.3-1. Comparison between short period gratings and long period gratings

	Short Period Gratings	Long Period Gratings
Grating period	0.5 - 1.0 μm	100 - 500 μm
3 dB bandwidth of reflected/attenuated wavelength	≈ 1 nm	≈ 10 nm
Back-reflections?	Yes	Negligible

mechanics used in this study; an applied coating of metal on the outside of the LPG fiber sensor causes a shift in the attenuated wavelengths within the cladding. As corrosion occurs, a change in the index of refraction will cause the attenuated wavelengths to shift back.

Figure 3.3-7 shows normalized frequency versus normalized propagation constant for several LP_{lm} core modes.[41] The normalized propagation constant is defined as

$$b = \frac{\left[\frac{\beta}{k} - n_2\right]}{n_1 - n_2}, \tag{16}$$

where k is the free space propagation constant, and the normalized frequency is defined as

$$V = \frac{2\pi}{\lambda} \cdot a n_1 \sqrt{2\Delta}, \tag{17}$$

where a is the core radius, and

$$\Delta = \frac{n_1^2 - n_2^2}{2n_1^2} \approx \frac{n_1 - n_2}{n_1}. \tag{18}$$

When β/k equals n_2 (at the cladding), $b=0$, and when β/k equals n_1 (at the core), $b=1$. For our studies, only the LP_{01} mode is of interest. Hence, as wavelength increases (or normalized frequency decreases), the LP_{01} mode approaches the cladding. Restated, the longer wavelengths are coupled into the cladding more readily than

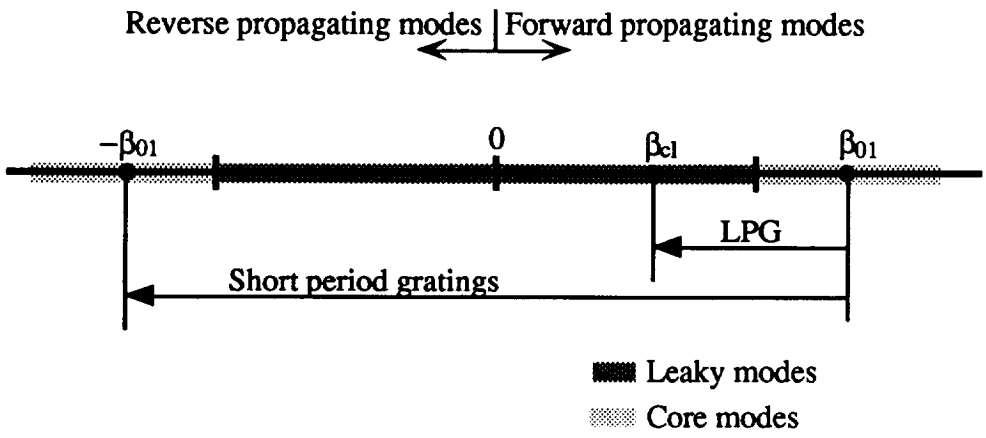

Figure 3.3-6. Conceptual propagation constant line for grating fabrication.

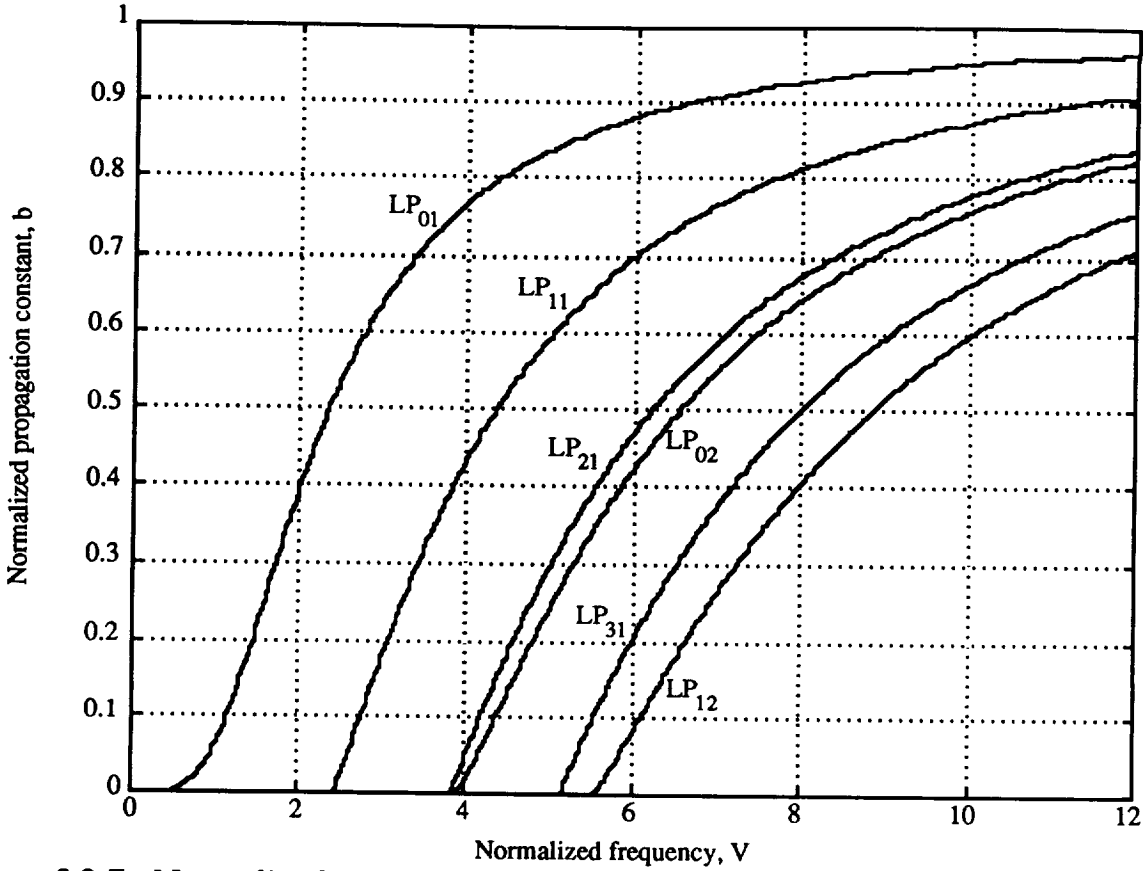

Figure 3.3-7. Normalized propagation constant vs. normalized frequency

the shorter wavelengths, for a given change in cladding properties. Hence, it can be predicted that there should be a greater shift in longer attenuated wavelengths than in shorter ones, for a given change in the medium surrounding the cladding region of the sensor. A similar set of curves exist for the cladding/jacket modes. The only difference in their derivation is that n_1 and n_2, the indices of refraction of the core and cladding, become n_2 and n_3, the indices of refraction for the cladding and jacket, or surrounding medium. Hence, the normalized frequency is defined as

$$V=\frac{2\pi}{\lambda} d n_2 \sqrt{2\Delta}\,, \tag{19}$$

where

$$\Delta = \frac{n_2^2 - n_3^2}{2n_2^2} \approx \frac{n_2 - n_3}{n_2}\,, \tag{20}$$

and d is the radius of the cladding region. Thus any change in d, n_2 or n_3 causes the V-number, and hence b for the cladding modes to change; the wavelength-selective

mode coupling occurs at a different wavelength and a change in the output spectrum is observed. If this shift in the attenuation bands can be measured, the external perturbation can be quantified. Hence, long period gratings provide a sensing mechanism whereby surface effects like corrosion can be monitored without pre-straining.

3.3.4. Corrosion Sensor Experimental Results

3.3.4.1. Strain Sensor Fabrication

A schematic of the extrinsic Fabry-Perot interferometer is shown in Figure 3.3-1. The type of optical fiber used in its construction is 1300 nm-wavelength, single mode, polyimide-coated fused silica quartz fiber, with a core diameter of 9 microns, a cladding diameter of 125 microns, and a coating thickness of 15 microns. The hollow core fiber is also polyimide-coated fused silica quartz, with an inner diameter of 190 microns, and an outer diameter of 295 microns.

To construct the sensors, a fabrication station was implemented, consisting of a microscope mounted above two fiber clamps, one of which was stationary, the other mounted on a three-axis micropositioner. The polyimide coating on the hollow core fiber was first removed using a razor blade, and cleaned with isopropyl alcohol. The end was hand-cleaved to achieve a relatively flat surface into which the fiber is fed. The hollow core fiber is locked in the stationary clamp. The single mode fiber is then stripped of its polyimide coating by burning it first with a lighter flame, and cleaning off the black residue with alcohol. The end is then cleaved using a commercially available fiber cleaver, to achieve an extremely flat endface, maximizing the amount of reflected light. The single mode fiber is cleaved in a manner so that the resulting two endfaces are both used in the sensor. Both fibers are fed into the hollow core fiber. The gap is set at approximately fifty microns. Knowledge of the exact dimension is not crucial, since the EFPI sensor measures relative strain; if the gap does not exceed half of the coherence length of the laser diode, the sensor will operate successfully.

Once the gap is set, epoxy is placed on the fibers, but is not wicked in as before; this would change the set gap, and also tends to pressurize the air inside the hollow core fiber, sometimes creating an air bubble in the glue joint and weakening the epoxy bond. The epoxy is again heated at 60 °C, until it has set; the sensor is then left in a desiccating chamber overnight, to allow the epoxy to completely cure.

3.3.4.2 Application of Metal Coating

Because the sensing mechanism in this study requires that a relatively thick coating of copper is applied to hold residual strain in the EFPI, several steps must be performed to apply a sufficient amount of metal. To ensure good adhesion to the glass hollow core fiber, sputtering or evaporation is employed to apply a thin initial coating of metal. Following either of these steps, electroplating is then utilized to apply thicker coatings. During the sputtering or evaporation phases, the sensors are not fixed in the strained position; it is only after either of these steps that any strain is applied. This is for several reasons:

- The sensors are easier to mount in the sputtering or evaporation chambers if they are free from strain.
- The risk of changing the incident strain on the sensors during transportation is eliminated.
- The risk of breaking the sensors is minimized.
- The sensors increase in strength following the application of a thin film of metal, allowing more pre-strain to be applied before electroplating.

This last point proved to be the most pertinent, since an attempt was made early in the study to pre-strain uncoated sensors, with catastrophic results. An overview of the sputtering and evaporation processes follows.

3.3.4.3 Physical Sputtering

Physical sputtering produces thin films of deposited metal with superior adhesion, compared to those obtained by evaporation or electroplating. The type of sputtering done for this research was performed in a radio frequency (RF) magnetron sputtering chamber. To apply thin coatings of metal, the sensors are either suspended one at a time in the chamber, or mounted on a stainless steel rack with polyimide tape. (The rack was originally designed to hold the sensors during the straining phase; it will be discussed later.) In either set-up, the sensors are placed between a target and a source gun. The target consists of the metal to be deposited on the substrate, the source gun functions as an electrode. The chamber is then evacuated, and back-filled with argon at approximately 10 millitorr. Argon is used due to its inert properties, and for its relatively large molecular size. The target and source gun are then connected to an RF voltage, and the argon gas is excited to the plasma state.

The principle of sputtering is that, as the argon atoms bombard the target with a high amount of energy, atoms of the target material are dislodged off the surface, and accelerate towards the source gun. In the process, some molecules strike the substrate and adhere to the surface. The purpose of using an RF source is that, at frequencies above 10 MHz, the highly mobile electrons in the plasma are able to

reach the anode, and hence become grounded, while the less mobile argon ions remain in the plasma. The end result is a nearly-continuous stream of argon ions bombarding the target.[42]

When the sensors were sputtered individually, the resulting thin film of copper was relatively free of oxide. Because the time to evacuate the system and sputter is quite lengthy, however, most of the sensors for this test were sputtered as a group on the stainless steel rack. To increase the spread of the sputtering gun, the chamber must be maintained at a higher vacuum. Unfortunately, when this was done, the amount of oxide deposited on the sensors increased; it is unknown what caused this increase in oxide deposition. As a result, some sensors were lost in attempting to coat copper over the oxide, since oxide layers contain much more surface stress than metal; upon contact with the plating solution, the oxide coating ruptured off of the surface of the sensor. For the latter tests, evaporation was used instead of sputtering.

3.3.4.4. Thermal Evaporation

The thermal evaporation process is simpler than sputtering, being both quicker and less expensive; the applied coatings are also traditionally thicker than those done using the sputtering process, although this attribute does not particularly impact this study. Even though the evaporation process does not provide the superior adhesion properties as sputtering, it was determined empirically that the amount of adhesion was sufficient for this study. The principal reason is that the entire sensor becomes encapsulated by the metal coating, helping to hold the residual strain on the hollow core fiber.

The target sensors are suspended in a vacuum bell jar as shown in Figure 3.3-8, with a tungsten holder, or boat, underneath them attached to high voltage electrodes. The chamber is filled with oxygen at a pressure of about 20 millitorr, and a plasma is ignited through the entire chamber, known as glow discharge cleaning. This helps to clean the substrate sensors, by heating the surface, and by breaking up surface hydrocarbons much like in sputtering. The chamber is then evacuated to a pressure of 5×10^{-5} torr or lower, to reduce the amount of deposited oxide. The tungsten boat is heated by supplying a high voltage to the electrodes; the copper melts and evaporates at room temperature, due to the lower operating vapor pressure, and is deposited on the suspended sensors. The support on which the sensors are attached is rotated, to apply an even coating over the entire surface of the sensors. A deposition rate of 22 Å is maintained, at a deposition distance of approximately fourteen inches.

Upon removal from the bell jar, the sensors have a bright, clean looking surface; there was no evidence that the coating was heavily oxidized. However, because the

coating is extremely thin, care must be taken to quickly apply a thicker coating of copper through electroplating, to avoid any build-up of a more resistive oxide layer.

3.3.4.5. Electroplating Deposition

To apply thicker coatings of metal, electroplating is the method of choice in metallurgy. The primary requirement for electroplating, however, is that the substrate be electrically conductive. Not only does evaporation and sputtering fulfill this requirement, but the adhesion characteristics of both are reliable. The electroplating process operates much like a conventional wet-cell battery, such as those in automobiles. The plating solution consists of the following ingredients:

- Copper sulfate ($CuSO_4$), 240 grams per liter
- Sulfuric acid (H_2SO_4), 15 grams per liter
- Thiourea, 0.001 grams per liter (used as a grain refiner, to decrease metal grain porosity, by forcing the grains to grow parallel to the substrate)
- Wetting agent, 0.1 grams per liter (used to maximize coverage of substrate, can be substituted with Ivory® dishwashing liquid)
- Brightener, 1 milliliter per liter (also a grain refiner, can be substituted with black strap molasses)

The setup for electroplating is shown in Figure 3.3-9. A piece of high-purity copper (A) is placed into the plating solution and is attached to the anode of a current-controlled power supply (B). The cathode is connected to the substrate, in this case the copper coated sensor (C), and is immersed in the solution. Solid contaminants are removed from the solution using a filtration system (D) much like those found in household aquariums. The solution agitation is maintained using a magnetic stirrer (E). The plating solution acts as an electrolyte, closing the circuit. Positive copper ions in the plating solution are attracted to the negatively charged substrate, adhering to the surface.

Several variables affect the adhesion, grain size, and rate of deposition of the plated copper: (1) the current density supported by the substrate, (2) the composition and concentration of the plating solution, (3) the relative location of the sensors with respect to themselves and the anode, and (4) the conductivity of the metal coating on the sensors. Because the exposed surface area of the sensors is very small, the applied current must be maintained at a relatively low level; should it becomes too high, there would be a reduction in adhesion and overall quality. However, if the current density is not maintained above a certain level, the sensors will not be

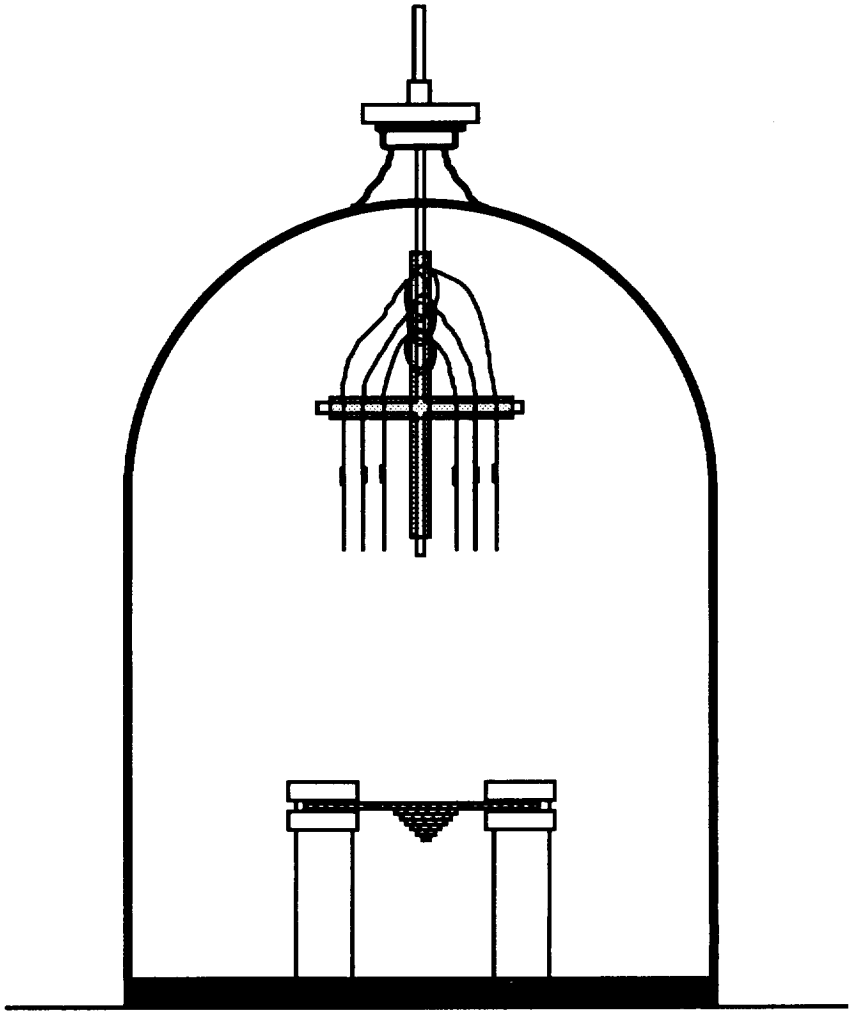

Figure 3.3-8. Thermal evaporation setup

sufficiently negatively charged, and the thin coatings will dissolve into the plating solution. The amount of applied current was generally between twenty and forty millamperes depending on the amount of exposed, activated copper. Also, if a sensor is too close to other sensors during electroplating, electromagnetic field lines emanating from the sensors can cause cathodic shielding, and as a result, uneven copper deposition.

3.3.4.6. Application of Stress

Before the sensors are mounted on the stainless steel rack used to apply stress, the sensors are connected to the cathode of the plating system, and a thin coating of

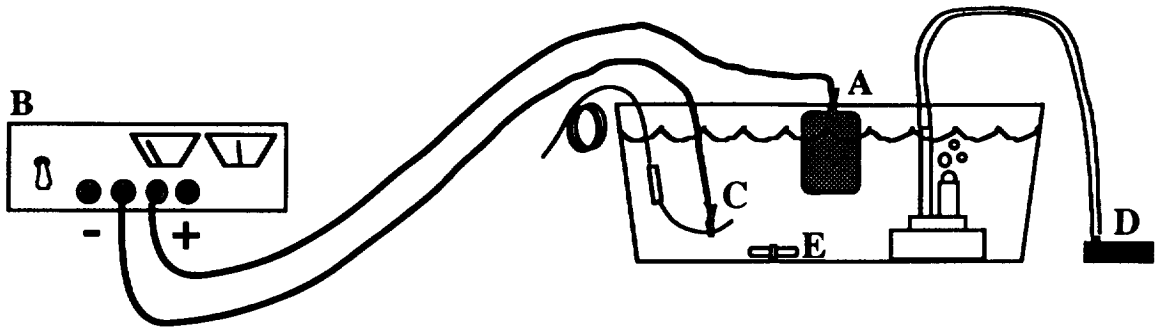

Figure 3.3-9. Electroplating setup

copper is applied. This is done to ensure a low-oxide, low-resistance layer of copper is present, before the effort is made to mount and strain them. One reason that copper was used in this study is that copper oxide is still conductive, unlike other materials such as aluminum. Due to high oxide surface stresses, applying a thin coating of copper ensures that the first layer of copper remains intact during the plating process, as discussed earlier.

After the sensors have a plated copper coating of about two microns in thickness, they are mounted onto the stainless steel rack. This procedure is the most significant one in attaining functional corrosion sensors, and also the one that required the most re-design throughout this research. The setup for this straining step is illustrated in Figure 3.3-10. Miller-Stephenson MS-907 epoxy (A) is used to adhere the sensor (B) to the stainless steel rack (C). Once completely hardened, the sensors are stressed by moving the sliding member (D) up with a stainless steel nut (E). An additional nut (F) is used to lock the moving member in place. The sensors are electrically connected to the rack with silver colloidal suspension (G).

It was discovered empirically that the copper does not adhere well to the epoxy joints at each end of the sensor. This lack of adhesion posed the problem that, if all the copper separates from these epoxy joints, the electrical connection between the rack and the hollow core fiber of the sensor is interrupted, not allowing plating to proceed. Also, if the sensor epoxy joints are only partially covered with copper, these small connections must support a higher current density, making them susceptible to burning. To alleviate this problem, silver paint was also applied to the epoxy joints of the sensor, and all the exposed fiber up to the stainless steel rack, on both sides of the sensor, to ensure that good electrical contact was maintained.

The entire rack was electrically connected to the plating system through a wire connection (H), and the lead-out fibers were protected from accidental detachment by fastening them to the rack with polyimide tape (J). Since the entire rack is

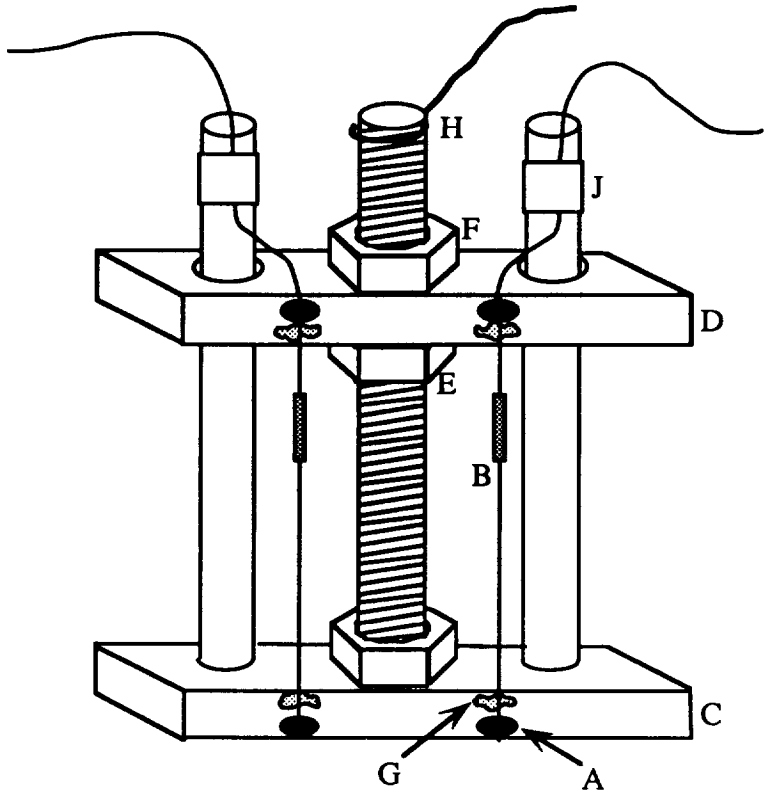

Figure 3.3-10: Stainless steel straining rack

electrically connected to the cathode, upon immersion into the plating solution, copper would begin to plate onto the stainless steel rack, as well as the sensors. This would deplete the supply of copper in the plating bath very quickly. To prevent this from happening, the entire rack (except for the sensors) was painted with a thick coating of plating protection liquid, commercially available as StopOff®. This protection liquid behaves much like nail polish; it dries very quickly, and will dissolve in acetone. (It is even bright red in color!) Its principal trait is that it remains inert in most acids, does not contaminate the plating solution, and acts as an electrical insulator.

3.3.4.7 Role of Epoxy Adhesion

The governing factor in determining the final thickness of the electroplated copper, and hence the amount of stored strain in the sensor, was the Miller-Stephenson MS-907 epoxy used to bond the sensors to the rack, and its ability to maintain good adhesion throughout the entire plating phase. Several steps were taken to aid in this adhesion:

- The surface of the stainless steel rack where the fiber was mounted was first roughened with a razor blade, and then cleaned with isopropyl alcohol.
- The bead of epoxy was rather large compared to the size of the fiber, approximately one centimeter in diameter, to increase the surface area of epoxy on the rack.
- The sensor fiber was secured onto the rack with a small piece of tape, to immobilize the fiber during the epoxy cure.
- Another sacrificial piece of optical fiber was placed underneath the sensor fiber, to raise the fiber up and ensure that the entire surface of the sensor fiber was encapsulated in the MS-907 epoxy. This was in lieu of having the sensor fiber rest on the surface of the rack during the cure, and not allowing the fiber to be completely covered in epoxy.
- After the epoxy was completely cured, the entire bead was painted over with a thick coating of StopOff®, to help isolate the epoxy from the plating bath; long period exposure to sulfuric acid is known to compromise the adhesion properties of MS-907 epoxy.[43]

These additional measures were partially successful; however, over a twenty-four-hour period in the plating bath, the strain decreased from an approximately 0.1% before immersion into the bath, to almost no strain upon removal from the bath. The results of this loss of adhesion will be presented later.

3.3.4.8. Corrosion of Metal Coated Strain Sensors

For the purpose of this study, corrosion is characterized as a decrease in the volume of metal. While this could be interpreted as a somewhat naive definition, it is sufficient for the scope of this study. Unfortunately, due to time constraints, the corrosion could not be modeled using more typical means, such as long-term salt spray atmospheric tests. Instead, the sensor's metal coating was removed at a constant rate over approximately one hour (depending on the test) using a corrosion medium consisting of a mixture of 10% nitric acid, 20% acetic acid, and 70% phosphoric acid. This mixture was used for its ability to give a very even rate of corrosion; it is typically used in the electroplating industry as a brightening agent.

3.3.4.9. Determination of Sensor Corrosion Rate

The corrosion rate was determined empirically, by generating a thickness-versus-time curve for several types of corrosion situations. These curves were used along with the known beginning thickness of metal coating on the sensor element to determine the corrosion rate for each sensor test. The corrosion rate curves were developed by first coating a piece of hollow core fiber with copper. The coated hollow core fiber was then placed in the corrosion bath for a set amount of time,

removed, and rinsed off with de-ionized water; the thickness of copper was then measured using a laser micrometer, since mechanical micrometers have a tendency to break the hollow core. These steps were performed in three different tests; the first on a piece of unstrained coated hollow core fiber, the second on a piece of hollow core fiber that was placed under strain during electroplating, and the third on a piece of hollow core fiber under strain, in an agitated solution. Liquid agitation was accomplished using a spinning bar magnet stirrer and stir plate, set to 30% of the maximum spinning rate.

The corrosion rate curves are shown in Figure 3.3-11. As expected, the corrosion rate increased for the situations in which the hollow core was strained, as well as for an agitated situation. In most of the corrosion tests performed on the sensors, the corrosion solution was agitated at 10% to prevent the sensor from being perturbed. During each test, the sensor was immersed completely in the solution, and testing continued until all the copper was removed from the surface, usually within two hours, depending on the initial thickness of copper.

3.3.4.10. EFPI Corrosion Sensor Test Results

A total of ten EFPI sensors were tested, all of which had been held in stress during the electroplating process. Although final results were obtained for ten sensors, approximately thirty sensors were fabricated to be subjects in this corrosion study; however, ten of these could not be used due to design flaws, and about ten more failed either during the straining or coating phase. What follows is a synopsis of the test results for the ten EFPI sensors that survived.

The first three sensors were tested, and a written description of the output trace was recorded as the tests progressed. In actuality, there were originally four sensors which were to be tested; however, one sensor broke while attempting to measure the thickness of copper on the hollow core with a set of mechanical micrometers. This method of measuring the coating thickness was later abandoned, for fear of breaking too many sensors. The three remaining sensors were then all corroded in an agitated solution, and from the fringe information and sensor gauge length, the strain release curves seen in Figure 3.3-12 were developed. Conflicting results exists for these three sensors; the sensor with the least amount of copper coating took the longest time to show a complete response. However, the third sensor showed the greatest amount of strain release, and was also the quickest to corrode. This follows since the copper coating would have been under more compressive strain, corroding faster due to stress corrosion. It should also be noted that the fringe contrast of the output signal (defined as the peak-to-peak voltage level of the EFPI output signal) in two of the three cases increased over the testing period, supporting the assertion that the sensor was relaxing during the tests, decreasing the gap size and increasing the fringe contrast (refer to Figure 3.3-2).

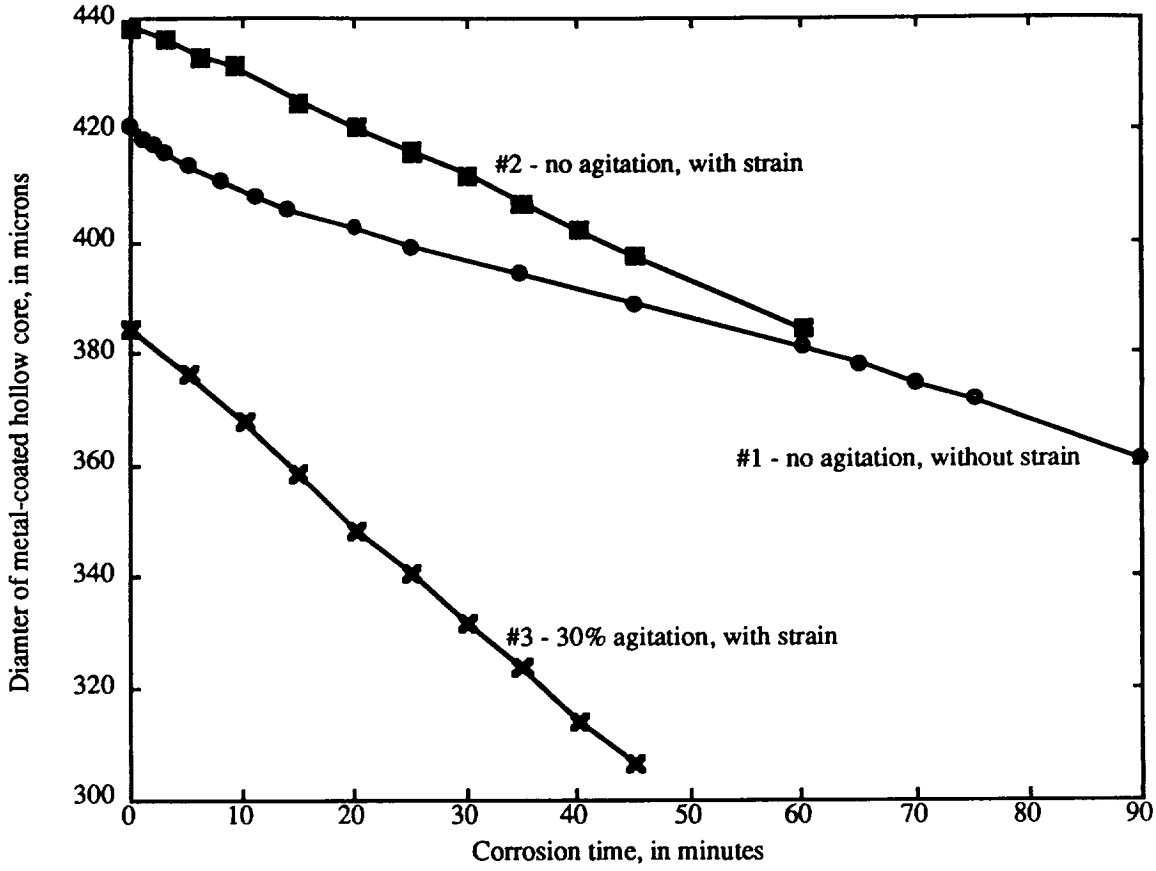

Figure 3.3-11. Results of corrosion rate tests

The next three sensors were tested in a similar fashion, except in a 10% agitated solution. The response was recorded on a digital sampling oscilloscope, and an attempt was made to store the traces for future use. Unfortunately, due to a bug in the oscilloscope firmware, the traces were lost. No additional data is available for these tests, except that the output showed multiple fringes during the corrosion cycle, as expected.

The final four sensors were corroded in the same manner as the previous three, except that a different method was used to acquire the data on the oscilloscope, and consequently none of the traces were lost. Since most of the fabrication, mounting and electroplating "bugs" were solved by the time these tests were performed, they resulted in being the most informative. The remainder of the experimental discussion on the EFPI corrosion sensors will focus on this final series of tests.

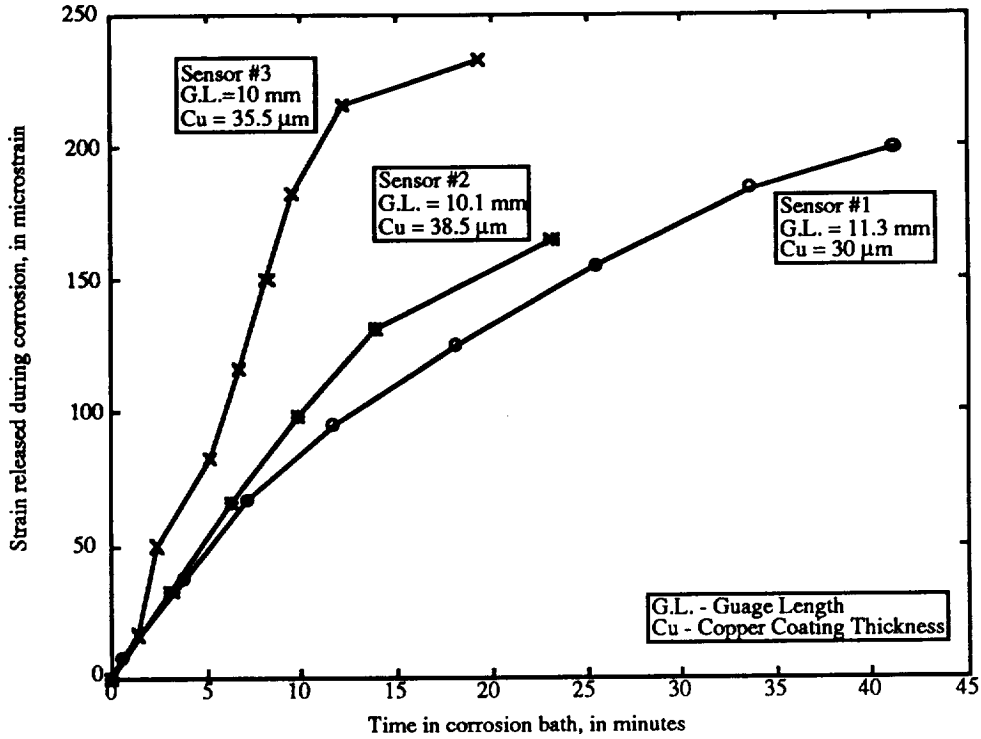

Figure 3.3-12. First EFPI corrosion sensor test results

The EFPI output traces of the final four sensors are seen in Figures 3.3-13 and 3.3-14 (in Figure 3.3-14(b), a bug in the data aquisition firmware resulted in loss of data for a few minutes, indicated as "loss of information" in the figure). All four of these sensors had approximately 50 microns of copper coating on the hollow core fiber. The differences in the number of interferometric fringes seen on the four sensors stem from two factors: the stainless steel rack used to pre-strain the sensors did not impart the same amount of strain on all the sensors, and also the gauge length for each sensor was different. Fifty microns of thickness was a sufficient amount of copper to hold the sensor in the strained position, despite the aforementioned challenges the stainless steel rack presented. To detach the sensors from the rack, a razor blade was carefully used to pop the epoxy bead off of the rack. In most cases, one of the glue beads was extremely easy to remove, and it was evident that plating solution had leaked past the StopOff®, and attacked the epoxy, since there was a small amount of copper that had plated onto the stainless steel rack *underneath* the epoxy bead. Also, there were some problems with the adhesion between the sensor fiber and the epoxy, but this loss of adhesion became negligible when the copper coating was removed from the polyimide-coated fiber; the adhesion between the copper coating and the polyimide is much worse than the adhesion between the polyimide and glass fiber.

An interesting phenomenon is observed in Figure 3.3-13 (a); first note that the initial eight minutes on the oscilloscope trace is not the response of the sensor to the corrosion bath, but to immersion in de-ionized water. This short test was conducted to observe the sensor's behavior to outside disturbances like liquid agitation, fume hood vibration, etc. Some drift occurred, but this is considered to be negligible. After eight minutes, the sensor was removed from the water and placed in the corrosion bath. Immediately, the sensor began to show a release of stored strain. Note that the rate of corrosion was slow at first (8-25 minutes) but then later increased as the coating of copper was removed (25-43 minutes). The reduction in the corrosion rate after 43 minutes is due to the fact that an insufficient amount of copper exists on the sensor to hold any more strain; although not pictured here, the oscilloscope trace remained at the same voltage level beyond 70 minutes. (This was true for the end of all the traces. Typically, the copper was completely removed during the last 5-10 minutes of the oscilloscope trace shown.)

Since the copper coating was applied as the sensor was relaxing (due to the aforementioned adhesion problems), the coating was under more compressive strain near the hollow core fiber than at the surface. It then follows that the rate of corrosion would be faster as the coating decreased, due to stress corrosion. Figure 3.3-13 (a) supports this hypothesis, evident from the increase in frequency of the oscilloscope fringes.

Another contributing factor that could have caused an increased response rate is wicking of corrosion solution under the copper coating, causing a loss in adhesion at the metal/glass interface. It is not known if this in fact took place, but one piece of evidence exists to support this hypothesis. Following the corrosion experiments, the sensors were examined under a microscope. In more than one case, the copper was completely removed from one side of the hollow core fiber, while the other side maintained a very thin coating, suggesting there was a preferential rate of corrosion over the circumference of the cylindrical hollow core. This could have been caused by corrosive liquid wicking in through the end of the sensor, and traveling down underneath the copper coating to the hollow core. However, this hypothesis is not completely airtight; because the solution was being agitated, it is possible that the medium was impinging upon one side of the sensor with more force than on another. Since insufficient evidence exists to support either of these ideas, it is unclear whether one, both, or neither of these factors caused a change in the sensor's response. What is not in question is that there is an increased rate of corrosion as the sensor loses its metal coating; by comparing the theoretical model to the actual data, for the same coating thickness and sensor parameters, it is apparent that the rate of corrosion is faster in the experimental results, as depicted in Figures 3.3-15, 3.3-16 and 3.3-17.

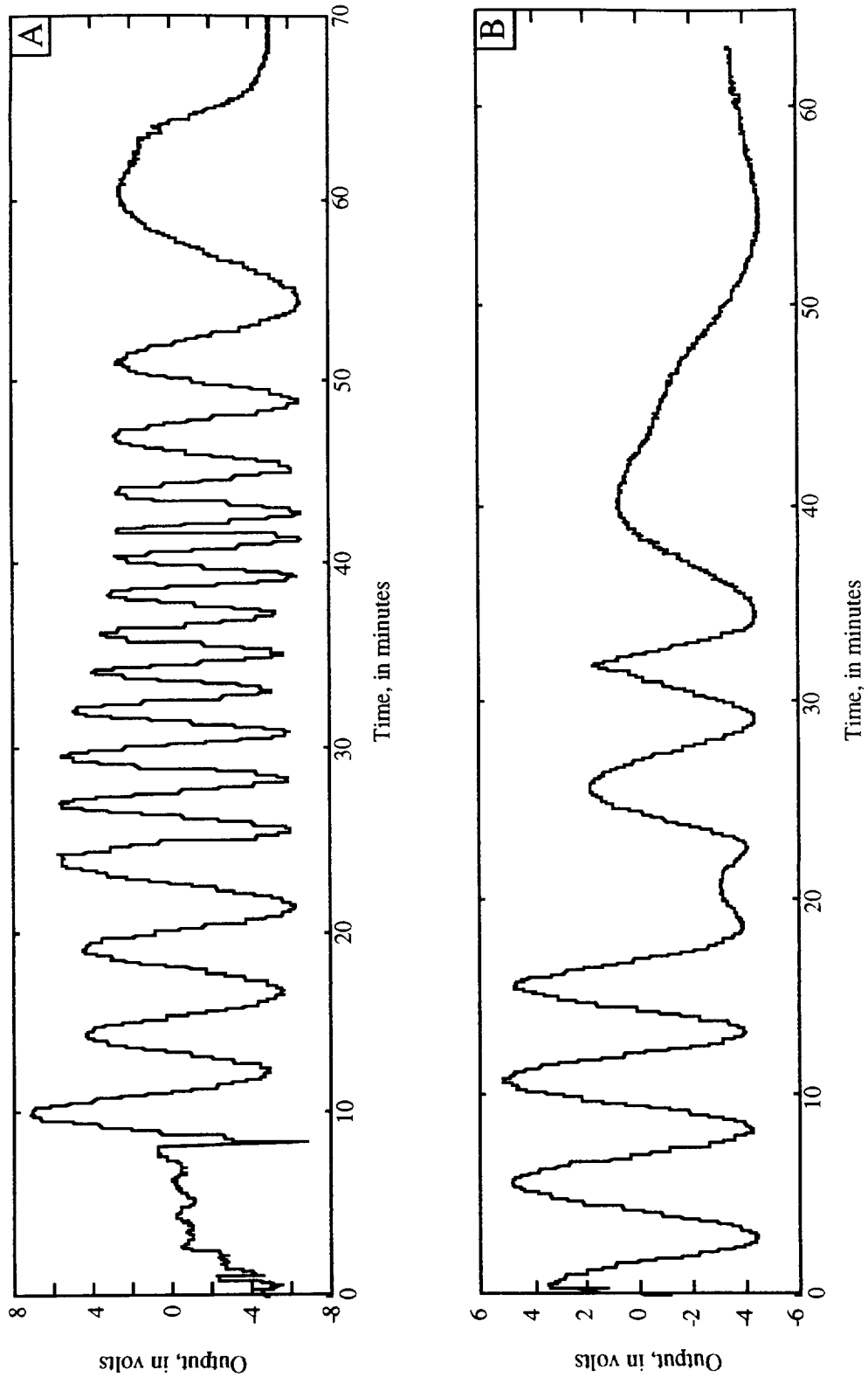

Figure 3.3-13 (a), (b). EFPI corrosion sensor test results

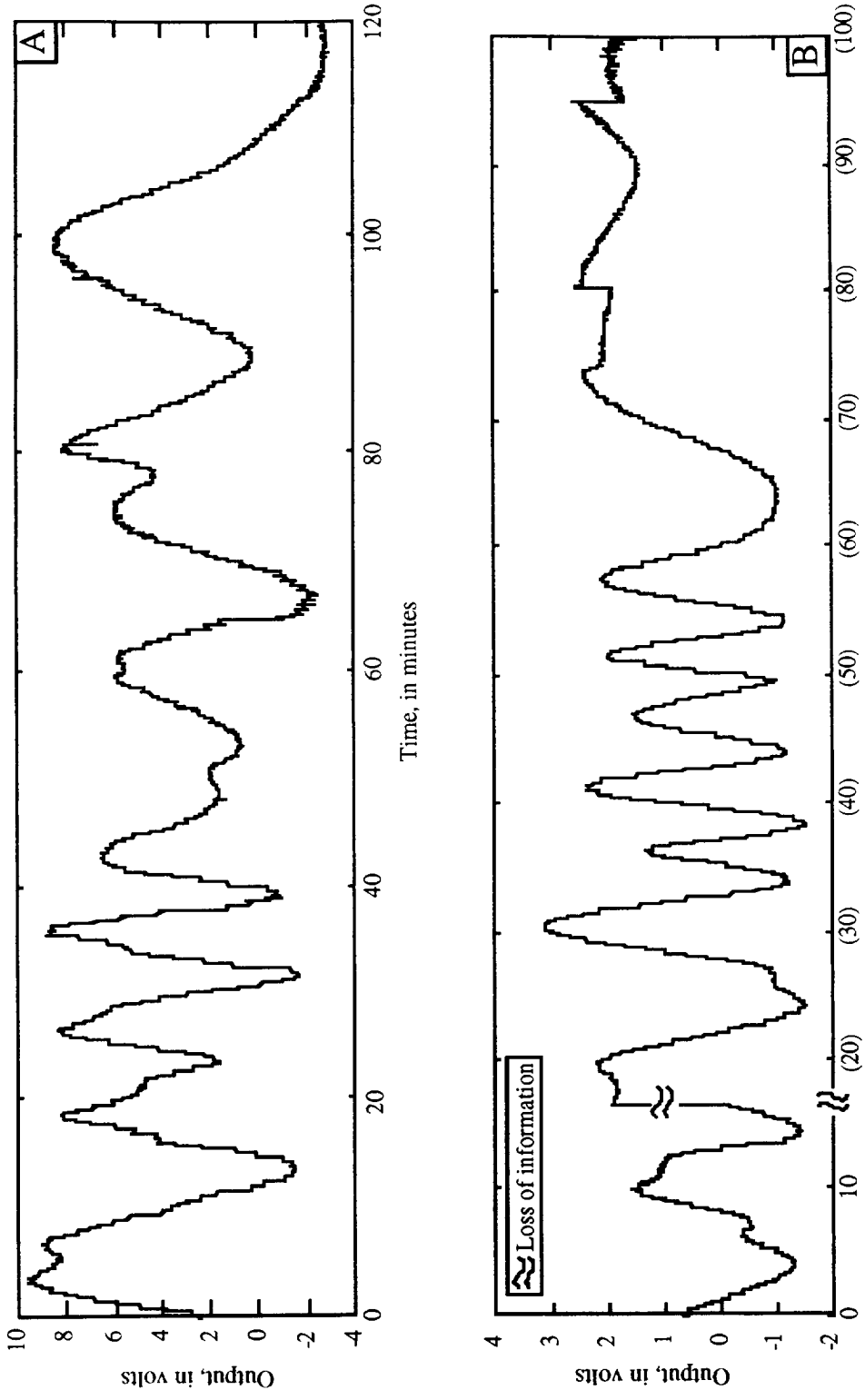

Figure 3.3-14 (a), (b). EFPI corrosion sensor test results

Figure 3.3-13 (b) does not exhibit the same increase in corrosion rate as Figure 3.3-13 (a), possibly because there are simply less fringes, an insufficient number to determine if there was an increase in the corrosion rate. More likely it is because there was simply not as much pre-strain on the EFPI sensor before plating, subduing the stress corrosion effect. This hypothesis is supported by examining each sensor's gauge length; since they both had comparable gauge lengths, they should exhibit a similar number of fringes for the same strain.

An interesting phenomenon occurs after twenty minutes in the corrosion bath; there is either a change in the direction of the EFPI sensor (a turn-around point), or an extensive amount of loss in the output signal. There is no evidence to support the presumption that this is a turn-around point; there is a hypothesis, however, to support the premise that there was a loss in signal power. Recall that the EFPI sensors that were fabricated for these tests were made with 155 micron diameter polyimide-coated single mode fiber, and 190 micron inner-diameter hollow core fiber. Hence there is 17.5 microns of leeway in either transverse direction for the single mode fiber to move around in; furthermore, the actual diameter of the single mode fiber with the polyimide coating removed is 125 microns, increasing the margin of mismatch between the fiber endfaces and the hollow core fiber to 32.5 microns in any direction. This large tolerance leads to alignment problems with the fiber endfaces; the more severe the misalignment, the less power that is received by the photodetector.

The proposed explanation for a severe decrease in the signal power at 20 minutes on Figure 3.3-13 (b) is that, as the sensor is relaxing, it is also becoming misaligned. This change in the output power is much more pronounced in Figure 3.3-14 (a). Further problems could be encountered if the endfaces of the EFPI sensor are not cleaved at right angles, aggravating any angular misalignment problems.[44] The misalignment in either case could be produced from a nonuniform rate of corrosion over the surface of the sensor, or from local disbonding of the copper coating on the surface of the hollow core fiber. The latter is more probable, since the surface of the coated sensors was found not to be uniform, as previously envisioned. Evidence of this can be seen in Figure 3.3-18, two scanning electron microscope pictures of an electroplated sensor before corrosion; these photographs show irregularities on the surface of electroplated sensors. These uneven protrusions could cause a local change in the amount of stored strain, possibly sufficient to cause alignment problems.

Finally, it should be noted that the loss of information in Figure 3.3-14 (b) causes the remainder of the data following the information gap to be somewhat misleading; the time axis is shown as being continuous, though the times would certainly be greater for a given point on the oscilloscope trace. The discontinuities seen after approximately 70 minutes were caused by factors outside of the corrosion bath, specifically, a change in the alignment of the splice tube used to join the sensor's input fiber to the EFPI support system, causing a DC-shift in the voltage trace.

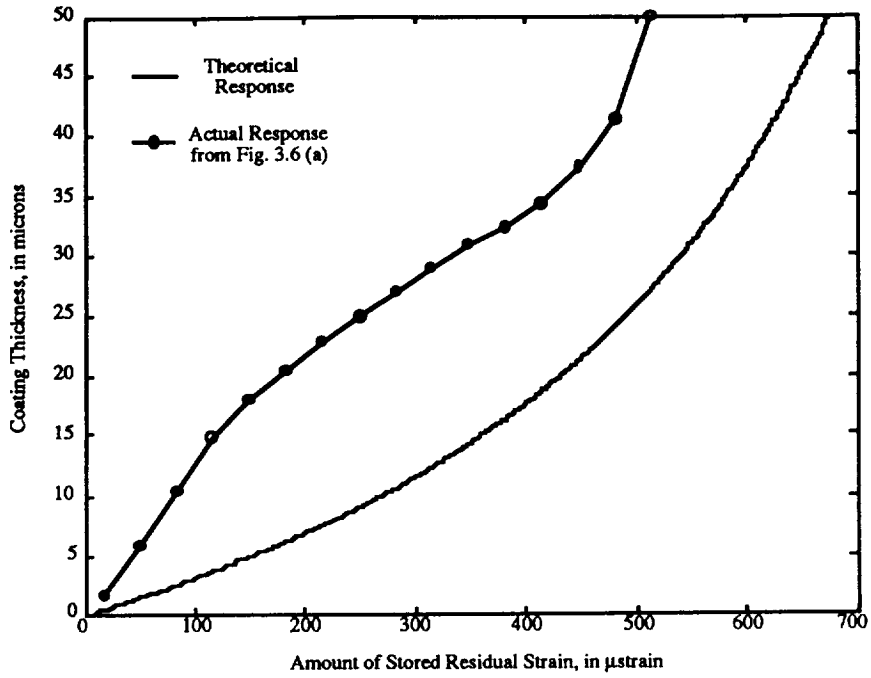

Figure 3.3-1515. Theoretical and experimental EFPI test results for Figure 3.3-13 (a).

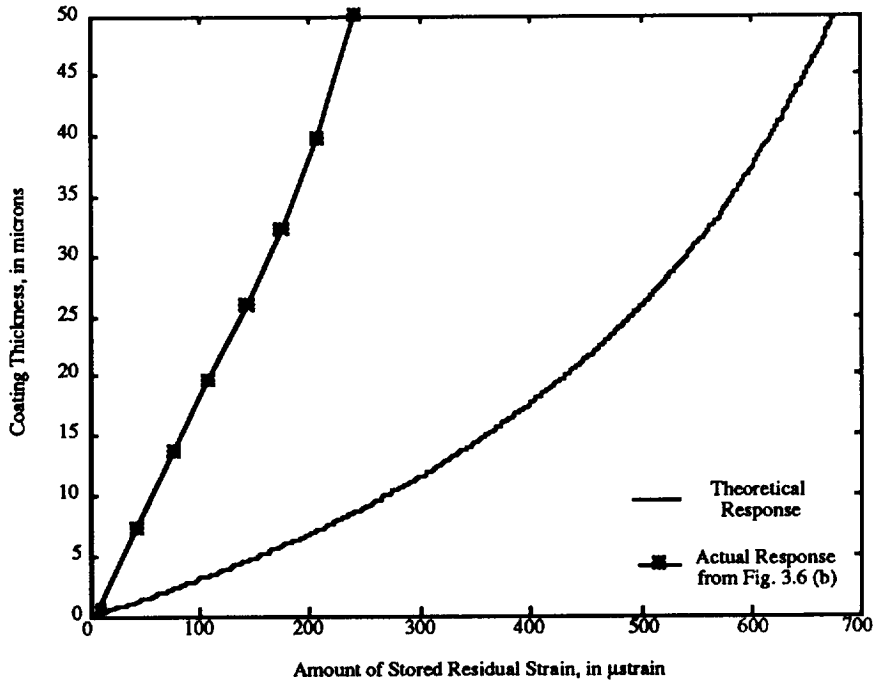

Figure 3.3-16. Theoretical and experimental EFPI test results for Figure 3.3-13 (b).

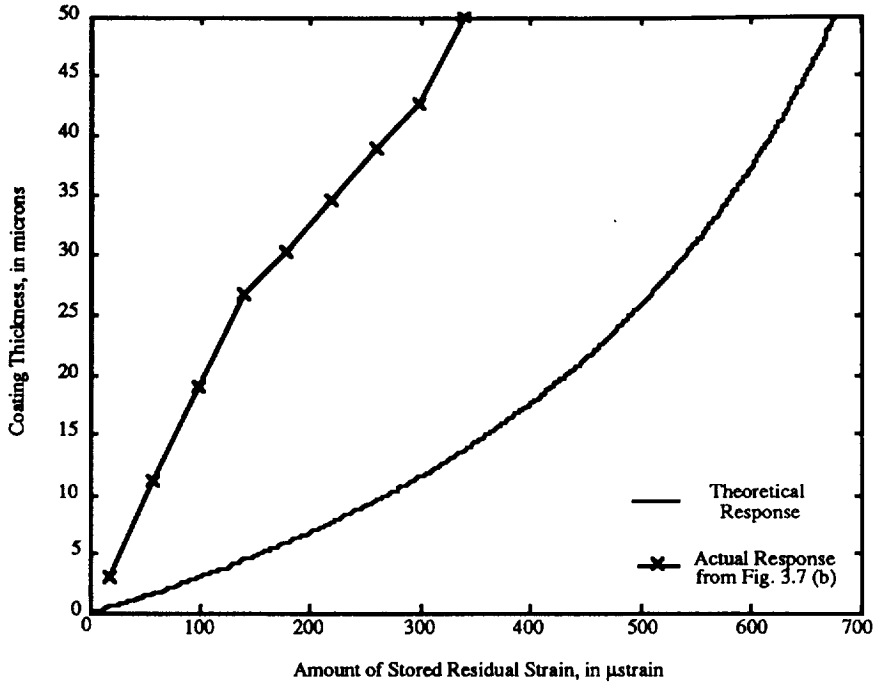

Figure 3.3-17. Theoretical and experimental EFPI corrosion test results for Figure 3.3-14 (b)

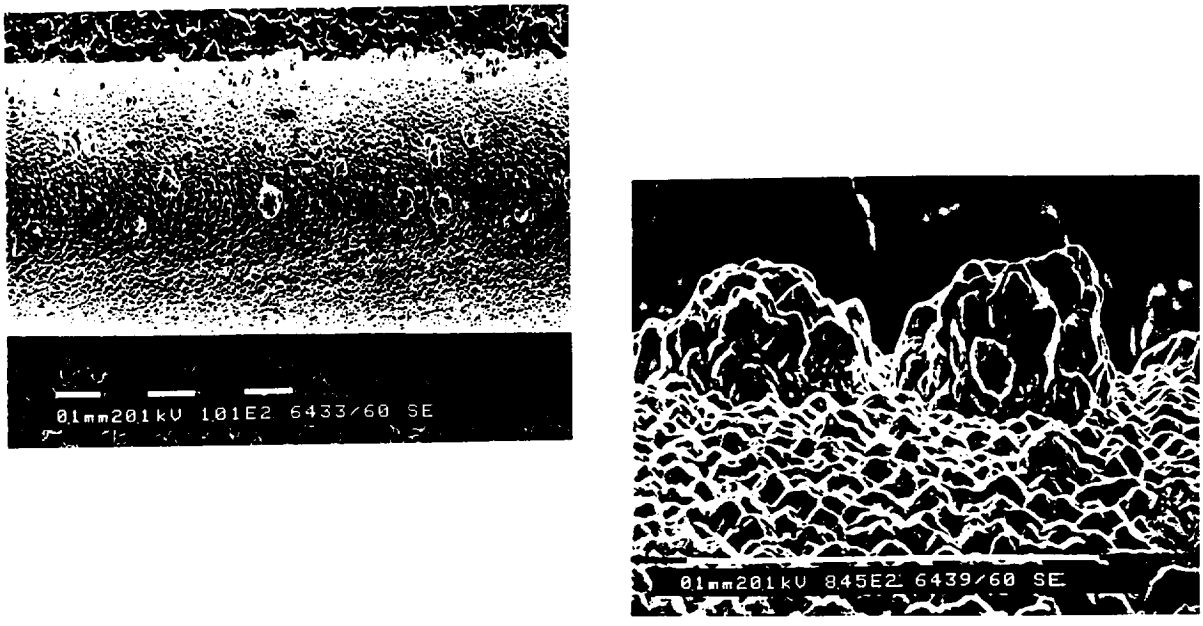

Figure 3.3-18. SEM photographs of copper coated strain sensor, before corrosion

3.3.5. Metal-Coated LPG Corrosion Sensor Experiments

The LPG corrosior. sensor measures the change in the index of refraction of the material surrounding the cladding when a metal coating is removed from the sensor. Hence, it was not necessary to take as many steps in preparing the sensors as with the EFPI strain sensors. Two LPG sensors were subjected to corrosion testing; one was tested once with an evaporated coating of copper, the other twice, first with an evaporated and electroplated coating of copper, second with an evaporated coating of nickel. Nickel does not corrode as readily in our corrosion bath; it was used primarily to show that the LPG corrosion sensor achieves results regardless of the metal used to coat the sensor. Because the interaction between the metal coating and evanescent cladding modes occurs only at the actual metal-glass boundary, it was not necessary to deposit very thick coatings of metal.

3.3.5.1. LPG Corrosion Sensor Test Results

The first test was with copper, and a thickness of fifteen microns was deposited. The sensor was then bonded to the stainless steel rack with Devcon® five minute epoxy. This was done only to ensure that the sensor remained in the straight position during the tests. Hardcopy traces were taken periodically throughout the tests; by overlapping the traces taken at the beginning and end of the tests, as shown in Figure 3.3-19, one can examine the attenuated wavelength shift. Since overlapping each trace would only confuse the issue, the results of the entire test are shown as in Figure 3.3-20. As the copper coating is removed, the LPG sensor is exposed to more of the corrosive medium, causing a change in the index of refraction at the cladding boundary, and hence causing the wavelength of the attenuated signal to shift. However, because the ambient medium changes from copper to the corrosion solution, the initial shift seen during corrosion is not of interest, since real-world situations would cause the sensor to be exposed to air, not the corrosion medium employed in this study. By removing the sensor from the medium after all the metal is corroded off and cleaning off any residual acid, the response of the sensor to air is determined, and compared to the response while coated with metal. Similar results are shown in Figures 3.3-21 and 3.3-22 for the other LPG sensor coated with copper, as well as the first sensor coated a second time with nickel. Comparing the two copper tests, note that although there was a thicker coating of copper on the first test, the time it took to remove all of the copper is less. As shown on the figures, the concentration of the corrosive solution was less for the second test; after performing the first test, subsequent tests were performed with a water-diluted corrosive solution, to slow the response time.

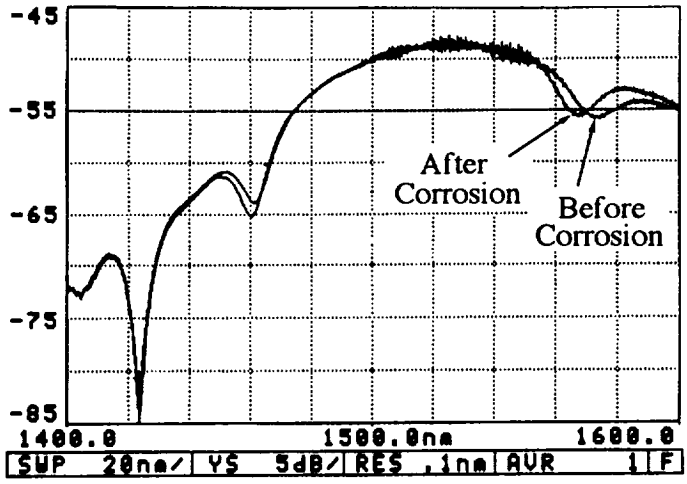

Figure 3.3-19. OSA traces of LPG corrosion test results

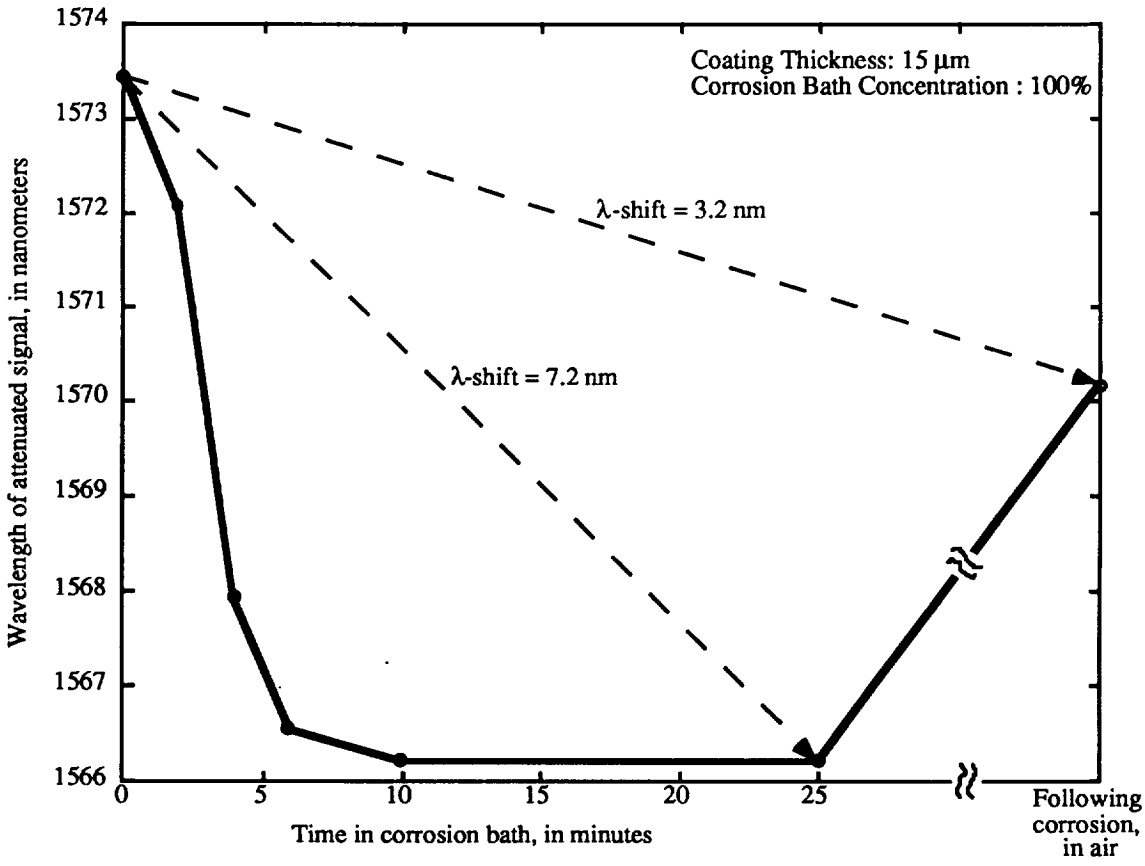

Figure 3.3-20. Overall results from LPG corrosion sensor test, copper coating.

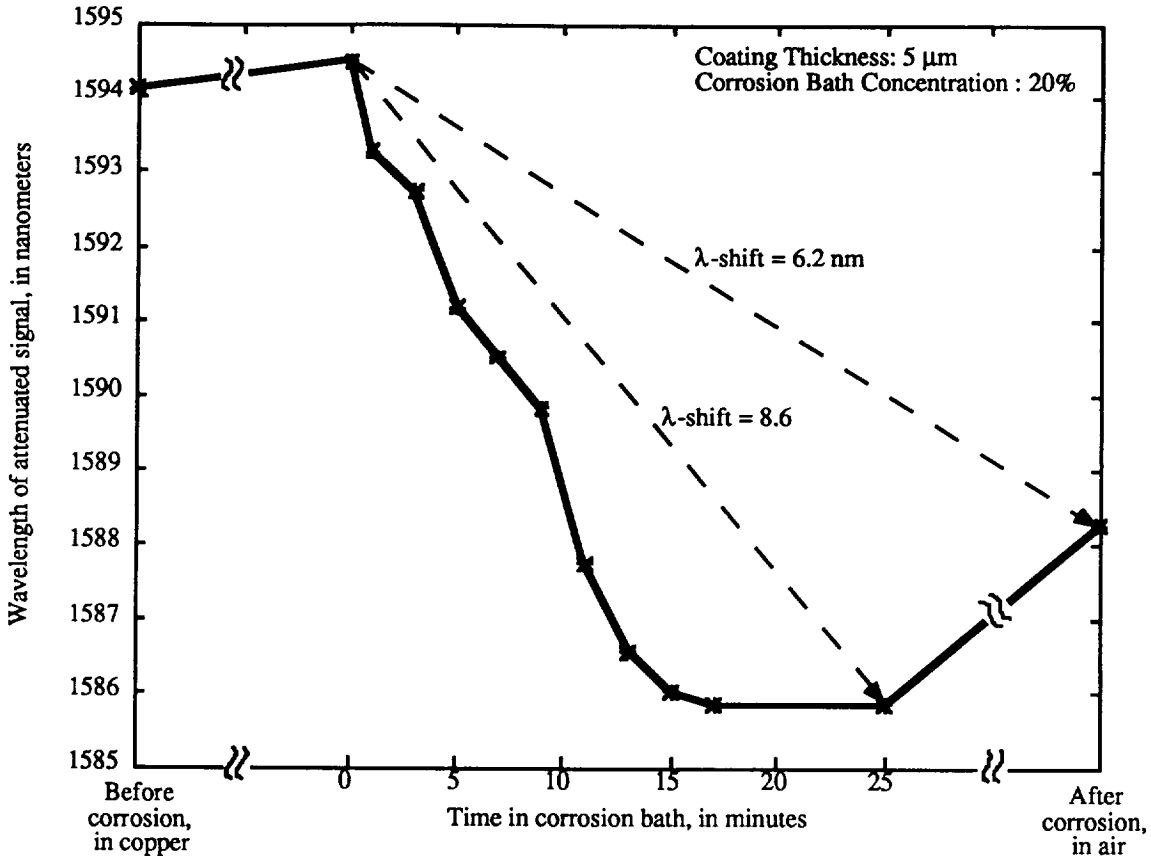

Figure 3.3-21. Overall results from LPG corrosion sensor test, copper coating.

All three tests showed that when the LPG sensor is coated with a metal, there is an increase in the wavelength of the attenuated signal. As the metal is removed, the wavelength of the attenuated signal decreases, the minimum amount being 1.7 nanometers. This wavelength shift is a discernible amount of change for standard methods of interrogation, such as with an optical spectrum analyzer or monochrometer. Some other experimental data[33] collected by researchers at the Fiber & Electro•Optics Research Center, shows the typical response of an LPG fiber sensor to different indices of refraction. The results of this test are shown in Figure 3.3-23. To properly interpret this graph, it should be noted that, as the index of refraction approaches that of the fiber, the output magnitude of the attenuated wavelength decreases; hence the data points around an index of refraction equal to 1.55 contain a large amount of error. The index of copper is much greater than that of glass, and the index of refraction of the corrosion solution is approximately 1.4. Hence, our tests correlate well with those obtained in the refractive index tests; the only point of debate is whether the response of the LPG sensors was on the left or

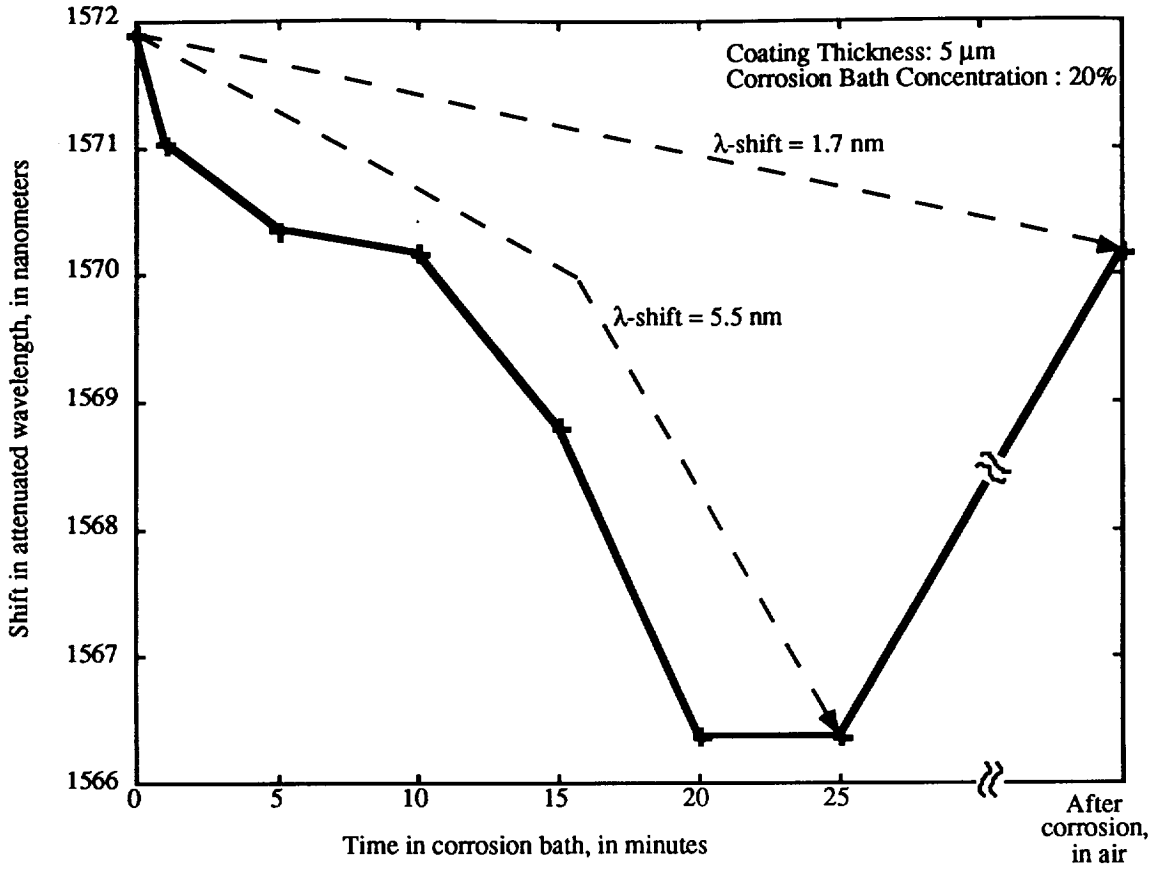

Figure 3.3-22. Overall results from LPG corrosion sensor test, nickel coating.

right side of 1.45 in Figure 3.3-23 during exposure to the corrosion bath. Based on the data obtained during corrosion, it is reasonable to assume that the response of the LPG sensor in the corrosive medium corresponds to the right side of 1.45, since the peak attenuated signal did not experience a minimum value during the corrosion tests. Since the sensor was removed very quickly from the corrosion bath and exposed to air, the response moved through the minimum value at an index of 1.45, to the value of 1.0 for air.

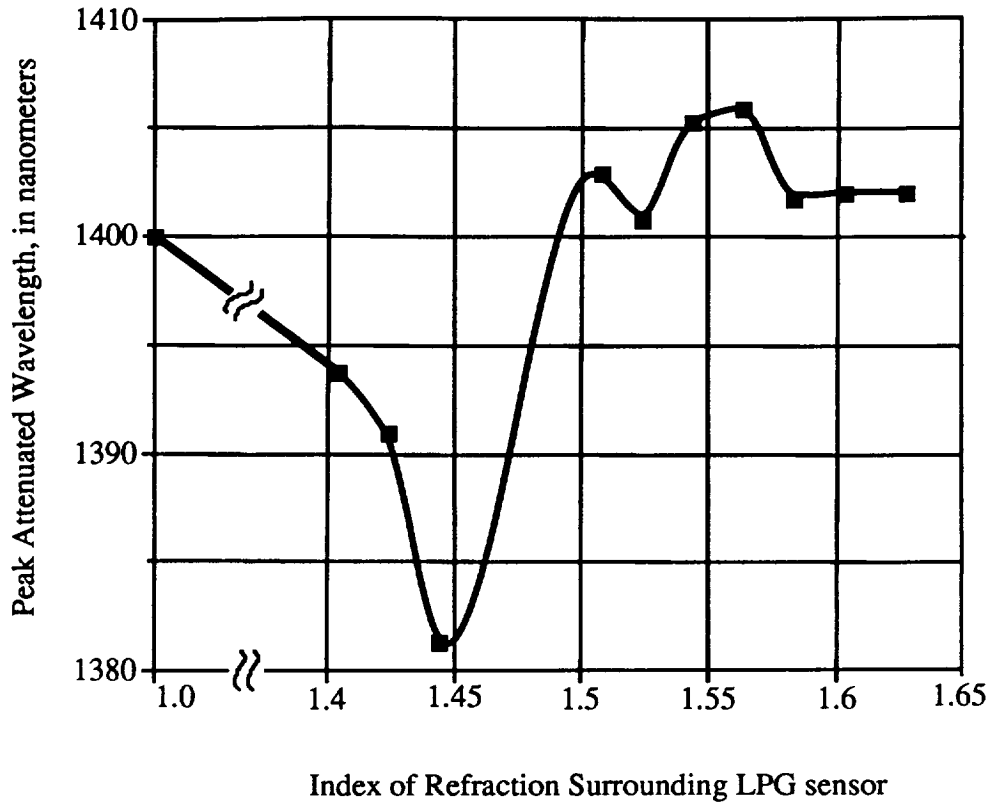

Figure 3.3-23. LPG sensor response to different indices of refraction

3.3.5. Conclusions and Recommendations for Fiber Optic Corrosion Sensors

This thesis study was successful in demonstrating a method of corrosion detection through the reduction in mass of a metal coating on the surface of fiber optic sensors. Two principal corrosion monitoring techniques were employed, one based on the ability of a thick metal coating to maintain residual strain in a fiber optic strain sensor, namely the extrinsic Fabry-Perot interferometer, the other based on the change in the index of refraction a coating of metal imparts upon the cladding region of a long period grating fiber optic sensor. Several points for improving strain sensor loading include:

- Redesign sensor strain rack to eliminate problem of sensor relaxation during the plating phase. Some ideas include to make the ends on the rack cylindrical, instead of rectangular, so that the lead in fiber and reflector fiber of the strain sensors can be wrapped around several times, using friction and possibly a small amount of adhesive to hold the sensors during straining.

- Improve upon the current method of applying strain; the single threaded bolt on the stainless steel rack does not apply even strain across several sensors at this time. One idea is to employ two smaller threaded pieces, to replace the current smooth bolts on which the sliding piece moves.
- In construction of the sensors, as well as that used to hold the sensors on the rack, utilize an adhesive that is not attacked by the acids found in plating solutions. The MS-907 epoxy is susceptible to acid attack, and will disbond or weaken.

Upon solving the adhesion problems encountered in this study, more metal can then be applied for a given amount of pre-strain. It is expected that this would then result in a sensor with more residual strain storage, giving a greater response.

Another important detail that should be restated is the need to test this technology using more traditional corrosion testing techniques; these include salt-spray tests, or fog tests, as described in ASTM procedures[34]. These types of tests are more acceptable for corrosion testing because they better model actual atmospheric conditions that are found in practical environments. Several interesting facets of corrosion are present in these tests that were absent from this study. They include (1) the response of LPG sensors as the thin coating of metal simply oxidizes, before any reduction in material mass occurs, (2) the affect corrosion by-products have on the strain response of EFPI sensors, and whether or not relaxation would occur at all, and (3) the response of either type of sensor when mounted on a surface undergoing corrosion, possibly including non-uniform corrosion over the surface of the sensor.

One might question the value of demonstrating corrosion sensing for copper, when most of the interest in corrosion detection (at least for the sponsors of this research) is in aluminum. This preliminary study was specifically designed to produce a metal corrosion sensor; copper was simply the easiest metal to deposit on the surface of the sensor, as well as to electroplate. Aluminum develops an insulating oxide layer very quickly, making electroplating extremely difficult. Should future research be conducted on this subject, one of two courses of action seem required; either perform the same kinds of tests on aluminum coated sensors, examining additional characteristics of corrosion that might not be present in copper, or continue examining ways to implement aluminum corrosion detection with copper coated (or another metal) sensors, and attempt to correlate sensor response to the corrosion parameters of aluminum. This method could be possible as more advancements in sensor architecture develop or different metal deposition ideas evolve. It is more likely, though, that the most feasible way would be to master the methods of depositing thick coatings of aluminum on the sensors, to effectively interrogate aluminum corrosion.

4.0 Acknowledgments

The authors would like to acknowledge Dr. J. Ken Shaw of the Mathematics Department of Virginia Tech for helpful discussions and suggestions relating to the use of neural networks for location of impacts using optical fibers sensors.

5.0 Publications

Publications issued during the course of this program are:

"Location of Impacts on Composite Panels by Embedded Fiber Optic Sensors and Neural Network Processing," P. Schindler, J.K. Shaw, R.G. May, and R.O. Claus, SPIE Proceedings Vol. 2444, *Smart Sensing, Processing, and Instrumentation,* 26 Feb. - 3 March 1995, San Diego, CA, pp. 481 - 489.

"Neural Network Processing of Optical Fiber Sensor Signals for Impact Location," P. Schindler, J.K. Shaw, R.G. May, and R.O. Claus, *Materials for Smart Systems:* Symposium Held Nov. 28 - Dec. 2, 1994, Boston, MA, Materials Research Society, editors: Easo P. George, et al.

6.0 References

1. T.O. 33B-1-1, NAVAIR 01-1A-16, TM55-1500-335-23: Nondestructive Inspection Methods

2. MIL-A-83444: "Airplane damage tolerance requirements," Military Standard, July 1974.

3. Anstee, R.F.W: "An assessment of the importance of small crack growth to aircraft design," AGARD Conference on Small Crack Growth, September 1982, pp. 3.1-3.9.

4. Eleftherton, P.M., and R. Fisher: "Monitoring of F-15 cracking with acoustic emission," Wright Research and Development Center, OH, pp. 91-94.

5. Scala, C.M., and R.A. Coyle: "Acoustic emission waveform analysis to identify fatigue crack propagation in a Mirage aircraft," Journal of Acoustic Emission, vol. 6, no. 4, pp. 249-256.

6. MIL-A-8867C: "Airplane strength and rigidity ground tests," Military Standard, June 1987.

7. MIL-1530A: "Aircraft structural integrity program, airplane requirements," Military Standard, September 1972.

8. Pokorski, J.R., and B.R. Fisher: "Fatigue damage sensing using acoustic emission," Wright-Patterson AFB, OH, September 1991.

9. Scala, C.M., S.J. Bowles, and I.G. Scott: "The development of acoustic emission for structural integrity monitoring of aircraft," DSTO Aeronautical Research Laboratories, Melbourne, Australia, pp. 219-257.

10. Scala, C.M., S.J. Bowles, J,F. McCardle, L. Spender and B.C. Bishop: "AE monitoring of military aircraft," Non-Destructive Testing-Australia, vol.27, no. 1, pp. 4-8, January/February 1990.

11. Schmid, C.A., M.S. Miller, G.P. Carmen, K.A. Murphy, and R.O. Claus: "Delamination detection scheme incorporating optical fiber sensors," Proc. 1993 IEEE Region 3 Conference, Charlotte, NC, April 1993.

12. Mast, P.W., G.E. Nash, J. Michopoulos, R.W. Thomas, R. Badaliance, and I. Wolock: "Experimental determination of dissipated energy density as a measure of strain-induced damage in composites," Naval Research Laboratory, April 1992.

13. AC 43-4A: "Corrosion control for aircraft," Federal Aviation Administration Advisory Circular, pp. 91- 110, July 1991.

14. Gunther, M.F., A. Wang, B.R. Fogg, S.E. Starr, K.A. Murphy, and R.O. Claus: "Fiber optic impact detection and location system embedded in a composite material," SPIE, Boston, September 1992.

15. Tour of USAir Maintenance Facilities, Roanoke Regional Airport (Woodrum Field), Roanoke, Virginia, October, 1993.

16. P. Heimgartner, J. Weber, "Thin-Layer Activation for Detecting Minute Losses of Material due to Corrosion or Wear," Sulzer Technical Review, pp. 20-22, Vol. 72, No. 1, 1990.

17. J.A. von Fraunhofer, Concise Corrosion Science, Portcullis Press Ltd., London, 1974.

18. W.H. Ailor, Handbook on Corrosion Testing and Evaluation, John Wiley & Sons, New York, 1971.

19. W.L. White, H. Leidheiser Jr., "The Corrosion Coulometer - A New Corrosion Monitor for Steel Structures," Corrosion, Vol. 46, No. 8, pp. 653-661, August 1990.

20. Z. Szklarska-Smialowska, R. Krishnakumar, "Ellipsometry in Studies of Metallic Corrosion and Oxidation," M.G.S. Ferreira, C.A. Melendres, (Ed.), Electrochemical and Optical Techniques for the Study and Monitoring of Metallic Corrosion, Kluwer Academic Publishers, Dordrecht, 1991.

21. P. Heimgartner, J. Weber, "Thin-Layer Activation for Detecting Minute Losses of Material due to Corrosion or Wear," Sulzer Technical Review, pp. 20-22, Vol. 72, No. 1, 1990.

22. G.K.Brown, N. Rothwell, "Corrosion Surveillance for Continuous Pipeline Integrity Monitoring," *Corrosion Prevention & Control*, Vol. 40, No. 1, pp. 19-23, February 1993.

23. A. Legat, C. Zevnik, "The Electrochemical Noise of Mild and Stainless Steel in Various Water Solutions," *Corrosion Science*, Vol. 35, No. 5-8, pt. 2, pp. 1661-1663, 1993.

24. J.H. Payer, "Controlling Corrosion in the Process Industries," *Sensors*, pp. 8-16, Vol. 7, No. 4, April 1990.

25. S.K. Chawla, T. Anguish, J.H. Payer, "Microsensors for Corrosion Control," *Materials Performance*, Vol. 20, No. 5, pp. 69-74, May 1990.

26. W.H. Smyrl, M.A. Butler, "Corrosion Sensors," Interface, The Electrochemical Society, Vol. 2, No. 4, pp. 35-39, Winter 1993.

27. A. Chase, ""Real -Time" Monitoring of Contact Corrosion for Process Control Systems," 78th Annual Meeting of the Technical Section of the Canadian Pulp and Paper Association, Montréal, Québec, pp. 189-193, January 28 and 29, 1992.

28. J.M. Galbraith, "In-Service Corrosion Monitoring with Automated Ultrasonic Testing Systems," The International Arctic Technology Conference, The Society of Petroleum Engineers, pp. 341-347, Anchorage, May 29-31, 1991.

29. H. Goedecke, "Corrosion Surveys with the *UltraScan* Pig," *Corrosion Prevention & Control*, Vol. 37, No. 2, pp. 33-36, April 1990.

30. W.J.H. Bender, A Chemical Sensor Based on Surface Plasmon Resonance on Surface Modified Optical Fibers, Doctor of Philosophy Dissertation, Department of Chemistry, Virginia Polytechnic Institute and State University, 1992.

[31] M. Miller, Optical Fiber-Based Corrosion Sensor Systems, Doctor of Philosophy Dissertation, The Bradley Department of Electrical Engineering, Virginia Polytechnic Institute and State University, 1995.

[32] M.R. Sajan, T.S. Radha, B.S. Ramprasad, "Measurement of the Corrosion Rate of Aluminum in Sodium Hydroxide Using Holographic Interferometry," Optics and Lasers in Engineering, pp. 183-188, Vol. 15, 1991.

[33] P. Jernberg, "Corrosion Evaluation of Coated Sheet Metal by means of Thermography and Image Analysis," *Thermosense XIII*, SPIE Vol. 1467, pp. 295-302, 1991.

[34] J.S. Namkung, M. Hoke, R.S. Rogowski, S. Albin, "Detection of Aluminum Corrosion by Evanescent Wave Absorption Spectroscopy With Optical Fibers," Smart Structures and Materials Conference, San Diego, September 1995.

[35] S.H. Poland, Applications of Optical Fiber Sensors with Thick Metal Coatings, Master of Science Thesis, The Bradley Department of Electrical Engineering, Virginia Polytechnic Institute and State University, May 1994.

[36] K.A. Murphy, M.F. Gunther, A.M. Vengsarkar, R.O. Claus, "Quadrature phase-shifted, extrinsic Fabry-Perot optical fiber sensors," *Optics Letters*, Vol. 16, pp. 273-275, 1991.

[37] F.P. Beer, E.R. Johnston, Jr., Mechanics of materials, 2nd ed., McGraw-Hill, Inc., New York, 1992.

[38] R.G. Budynas, Advanced Strength and Applied Stress Analysis, McGraw-Hill, Inc., New York, 1977.

[39] R. Kashyap, "Photosensitive Optical Fibers: Devices and Applications," *Optical Fiber Technology*, Vol. 1, pp. 17-34, 1994.

[40] A.M. Vengsarkar, P.J. Lemaire, J.B. Judkins, V. Bhatia, J.E.Sipe, and T. Erdogan, "Long-Period Fiber Gratings as Filters and Spectral Shape-Shifters," Post-deadline paper, *Optical Fiber Communications Conference*, San Diego, California, February 1995.

[41] G. Keiser, Optical Fiber Communications, McGraw-Hill, Inc., New York, 1991.

42. J. Zeakes, Extrinsic Fabry-Perot Interferometric Hydrogen Gas Sensor, Master of Science Thesis, The Bradley Department of Electrical Engineering, Virginia Polytechnic Institute and State University, 1994.

43. Specifications Sheet, MS-907 epoxy, Miller-Stephenson, George Washington Highway, Danbury, Connecticut, 06810, (203) 743-4447, April 1995.

44. M.J.C. de Vries, Optical Fiber Sensors for Advanced Civil Structures, Doctor of Philosophy Dissertation, The Bradley Department of Electrical Engineering, Virginia Polytechnic Institute and State University, 1995.